Depth of maximum of air-shower profiles above $10^{17.7}$ eV measured with the fluorescence detector of the Pierre Auger Observatory

A. Abdul Halim,[13] P. Abreu,[67] M. Aglietta,[50,49] M. Ahmed,[31] I. Allekotte,[1] K. Almeida Cheminant,[75,74] R. Aloisio,[42,43] J. Alvarez-Muñiz,[73] A. Ambrosone,[42,43] J. Ammerman Yebra,[73] L. Anchordoqui,[79] B. Andrada,[7] L. Andrade Dourado,[42,43] L. Apollonio,[55,46] C. Aramo,[47] E. Arnone,[59,49] J. C. Arteaga Velázquez,[63] P. Assis,[67] G. Avila,[11] E. Avocone,[53,43] A. Bakalova,[29] Y. Balibrea,[11] A. Baluta,[70] F. Barbato,[42,43] A. Bartz Mocellin,[78] J. P. Behler,[10] J. A. Bellido,[13] C. Berat,[h] M. E. Bertaina,[59,49] M. Bianciotto,[39] P. L. Biermann,[a] V. Binet,[5] K. Bismark,[35,7] T. Bister,[74,75] J. Biteau,[33,j] J. Blazek,[29] J. Blümer,[37] M. Boháčová,[29] D. Boncioli,[53,43] C. Bonifazi,[16,8] N. Borodai,[65] J. Brack,[f] P. G. Brichetto Orquera,[7,37] A. Bueno,[72] S. Buitink,[15] A. Bwembya,[74,75] T. R. Caba Pineda,[37] K. S. Caballero-Mora,[62] S. Cabana-Freire,[73] L. Caccianiga,[55,46] J. Caraça-Valente,[78] R. Caruso,[54,44] A. Castellina,[50,49] F. Catalani,[18] G. Cataldi,[45] L. Cazon,[73] M. Cerda,[10] B. Čermáková,[37] A. Cermenati,[42,43] K. Cerny,[30] J. A. Chinellato,[21] J. Chudoba,[29] L. Chytka,[30] R. W. Clay,[13] A. C. Cobos Cerutti,[6] R. Colalillo,[56,47] R. Conceição,[67] G. Consolati,[46,51] M. Conte,[52,45] F. Convenga,[42,43] D. Correia dos Santos,[25] P. J. Costa,[67] C. E. Covault,[77] M. Cristinziani,[41] C. S. Cruz Sanchez,[3] S. Dasso,[4,2] K. Daumiller,[37] B. R. Dawson,[13] R. M. de Almeida,[25] E.-T. de Boone,[41] B. de Errico,[25] J. de Jesús,[73] S. J. de Jong,[74,75] J. R. T. de Mello Neto,[25] I. De Mitri,[42,43] D. de Oliveira Franco,[40] F. de Palma,[52,45] V. de Souza,[19] E. De Vito,[52,45] A. Del Popolo,[54,44] O. Deligny,[31] N. Denner,[29] K. Denner Syrokvas,[28] L. Deval,[49] A. di Matteo,[49] C. Dobrigkeit,[21] J. C. D'Olivo,[64] L. M. Domingues Mendes,[16,67] T. Dominguez,[1] Y. Dominguez Ballesteros,[27] Q. Dorosti,[41] R. C. dos Anjos,[24] J. Ebr,[29] F. Ellwanger,[37] R. Engel,[35,37] I. Epicoco,[52,45] M. Erdmann,[38] A. Etchegoyen,[7,12] C. Evoli,[42,43] H. Falcke,[74,76,75] G. Farrar,[81] A. C. Fauth,[21] T. Fehler,[41] F. Feldbusch,[36] A. Fernandes,[67] M. Fernández Alonso,[14] B. Fick,[80] J. M. Figueira,[7] P. Filip,[35,7] A. Filipčič,[71,70] T. Fitoussi,[37] B. Flaggs,[83] A. Franco,[45] M. Freitas,[67] T. Fujii,[82,i] A. Fuster,[7,12] C. Galea,[74] B. García,[6] C. Gaudu,[34] P. L. Ghia,[31] U. Giaccari,[45] M. Giammarco,[53,43] C. Glaser,[39] F. Gobbi,[10] F. Gollan,[7] G. Golup,[1] P. F. Gómez Vitale,[11] J. P. Gongora,[11] N. González,[7] D. Góra,[65] A. Gorgi,[50,49] M. Gottowik,[37] F. Guarino,[56,47] G. P. Guedes,[22] Y. C. Guerra,[10] L. Gülzow,[37] S. Hahn,[35] P. Hamal,[29] M. R. Hampel,[7] P. Hansen,[3] V. M. Harvey,[13] A. Haungs,[37] M. Havelka,[29] T. Hebbeker,[38] C. Hojvat,[d] J. R. Hörandel,[74,75] P. Horvath,[30] M. Hrabovský,[30] T. Huege,[37,15] A. Insolia,[54,44] P. G. Isar,[69] M. Ismaiel,[74,75] P. Janecek,[29] V. Jilek,[29] K.-H. Kampert,[34] B. Keilhauer,[37] V. V. Kizakke Covilakam,[7,37] H. O. Klages,[37] M. Kleifges,[36] A. Klingel,[29] J. Köhler,[37] F. Krieger,[38] M. Kubatova,[29] N. Kunka,[36] B. L. Lago,[17] N. Langner,[38] N. Leal,[7] M. A. Leigui de Oliveira,[23] Y. Lema-Capeans,[73] A. Letessier-Selvon,[32] I. Lhenry-Yvon,[31] L. Lopes,[67] J. P. Lundquist,[70] M. Mallamaci,[57,44] S. Mancuso,[50,49] D. Mandat,[29] P. Mantsch,[d] A. G. Mariazzi,[3] C. Marinelli,[42,43] I. C. Mariş,[14] G. Marsella,[57,44] D. Martello,[52,45] S. Martinelli,[37,7] O. Martínez Bravo,[60] A. Martínez-Mendez,[27] M. A. Martins,[29] H.-J. Mathes,[37] J. Matthews,[g] G. Matthiae,[58,48] E. Mayotte,[78] S. Mayotte,[78] P. O. Mazur,[d] G. Medina-Tanco,[64] J. Meinert,[34] D. Melo,[7] A. Menshikov,[36] C. Merx,[37] S. Michal,[29] M. I. Micheletti,[5] L. Miramonti,[55,46] M. Mogarkar,[65] S. Mollerach,[1] F. Montanet,[h] L. Morejon,[34] K. Mulrey,[74,75] R. Mussa,[49] W. M. Namasaka,[34] S. Negi,[29] L. Nellen,[64] K. Nguyen,[80] G. Nicora,[9] M. Niechciol,[41] D. Nitz,[80] D. Nosek,[28] A. Novikov,[83] V. Novotny,[28] L. Nožka,[30] A. Nucita,[52,45] L. A. Núñez,[27] S. E. Nuza,[4] J. Ochoa,[7,37] M. Olegario,[19] C. Oliveira,[20] L. Östman,[29] M. Palatka,[29] J. Pallotta,[9] G. Parente,[73] T. Paulsen,[34] J. Pawlowsky,[34] M. Pech,[29] J. Pękala,[65] R. Pelayo,[61] V. Pelgrims,[14] C. Pérez Bertolli,[73] L. Perrone,[52,45] S. Petrera,[42,43] T. Pierog,[37] M. Pimenta,[67] M. Platino,[7] B. Pont,[74] M. Pourmohammad Shahvar,[57,44] P. Privitera,[82] C. Priyadarshi,[65] M. Prouza,[29] K. Pytel,[66] S. Querchfeld,[34] J. Rautenberg,[34] D. Ravignani,[7] J. V. Reginatto Akim,[21] M. Z. Rennó,[21] A. Reuzki,[38] J. Ridky,[29] F. Riehn,[39] M. Risse,[41] V. Rizi,[53,43] B. Rocha Moldes,[73] E. Rodriguez,[7,37] G. Rodriguez Fernandez,[48] J. Rodriguez Rojo,[11] S. Rossoni,[40] M. Roth,[37] E. Roulet,[1] A. C. Rovero,[4] A. Saftoiu,[68] M. Saharan,[74] F. Salamida,[53,43] H. Salazar,[60] G. Salina,[48] P. Sampathkumar,[37] N. San Martin,[78] J. D. Sanabria Gomez,[27] F. Sánchez,[7] F. M. Sánchez Rodriguez,[73] E. Santos,[29] F. Sarazin,[78] R. Sarmento,[67] R. Sato,[11] P. Savina,[42,43] V. Scherini,[52,45] H. Schieler,[37] M. Schimp,[34] D. Schmidt,[37] O. Scholten,[15,b] H. Schoorlemmer,[74,75] P. Schovánek,[29] F. G. Schröder,[83,37] J. Schulte,[38] T. Schulz,[29] S. J. Sciutto,[3] M. Scornavacche,[7] A. Sedoski,[7] S. Sehgal,[34] S. U. Shivashankara,[70] G. Sigl,[40] K. Simkova,[15,14] F. Simon,[36] R. Šmída,[82] S. Soares Sippert,[25] P. Sommers,[e] S. Stanič,[70] J. Stasielak,[65] P. Stassi,[h] S. Strähnz,[35] M. Straub,[38] T. Suomijärvi,[33] A. D. Supanitsky,[7] Z. Svozilikova,[29] Z. Szadkowski,[66] F. Tairli,[13] A. Tapia,[26] C. Taricco,[59,49] C. Timmermans,[75,74] O. Tkachenko,[29] P. Tobiska,[29] C. J. Todero Peixoto,[18] B. Tomé,[67] A. Travaini,[10] P. Travnicek,[29] C. Trimarelli,[42,43] M. Tueros,[3] M. Unger,[37] R. Uzeiroska-Geyik,[34] L. Vaclavek,[30] M. Vacula,[30] I. Vaiman,[42,43] J. F. Valdés Galicia,[64] L. Valore,[56,47] P. van Dillen,[74,75] E. Varela,[60] V. Vašíčková,[34] A. Vásquez-Ramírez,[27] D. Veberič,[37] I. D. Vergara Quispe,[3]

S. Verpoest,[83] V. Verzi,[48] J. Vicha,[29] S. Vorobiov,[70] J. B. Vuta,[29] C. Watanabe,[25] A. A. Watson,[c] A. Weindl,[37] M. Weitz,[34] L. Wiencke,[78] H. Wilczyński,[65] B. Wundheiler,[7] B. Yue,[34] A. Yushkov,[29] E. Zas,[73] D. Zavrtanik,[70,71] and M. Zavrtanik[71,70]

(Pierre Auger Collaboration)

[1]*Centro Atómico Bariloche and Instituto Balseiro (CNEA-UNCuyo-CONICET), San Carlos de Bariloche, Argentina*
[2]*Departamento de Física and Departamento de Ciencias de la Atmósfera y los Océanos, FCEyN, Universidad de Buenos Aires and CONICET, Buenos Aires, Argentina*
[3]*IFLP, Universidad Nacional de La Plata and CONICET, La Plata, Argentina*
[4]*Instituto de Astronomía y Física del Espacio (IAFE, CONICET-UBA), Buenos Aires, Argentina*
[5]*Instituto de Física de Rosario (IFIR)—CONICET/U. N. R. and Facultad de Ciencias Bioquímicas y Farmacéuticas U.N.R., Rosario, Argentina*
[6]*Instituto de Tecnologías en Detección y Astropartículas (CNEA, CONICET, UNSAM), and Universidad Tecnológica Nacional—Facultad Regional Mendoza (CONICET/CNEA), Mendoza, Argentina*
[7]*Instituto de Tecnologías en Detección y Astropartículas (CNEA, CONICET, UNSAM), Buenos Aires, Argentina*
[8]*International Center of Advanced Studies and Instituto de Ciencias Físicas, ECyT-UNSAM and CONICET, Campus Miguelete—San Martín, Buenos Aires, Argentina*
[9]*Laboratorio Atmósfera—Departamento de Investigaciones en Láseres y sus Aplicaciones—UNIDEF (CITEDEF-CONICET), Argentina*
[10]*Observatorio Pierre Auger, Malargüe, Argentina*
[11]*Observatorio Pierre Auger and Comisión Nacional de Energía Atómica, Malargüe, Argentina*
[12]*Universidad Tecnológica Nacional—Facultad Regional Buenos Aires, Buenos Aires, Argentina*
[13]*Adelaide University, Adelaide, S.A., Australia*
[14]*Université Libre de Bruxelles (ULB), Brussels, Belgium*
[15]*Vrije Universiteit Brussels, Brussels, Belgium*
[16]*Centro Brasileiro de Pesquisas Fisicas, Rio de Janeiro, RJ, Brazil*
[17]*Centro Federal de Educação Tecnológica Celso Suckow da Fonseca, Petropolis, Brazil*
[18]*Universidade de São Paulo, Escola de Engenharia de Lorena, Lorena, SP, Brazil*
[19]*Universidade de São Paulo, Instituto de Física de São Carlos, São Carlos, SP, Brazil*
[20]*Universidade de São Paulo, Instituto de Física, São Paulo, SP, Brazil*
[21]*Universidade Estadual de Campinas (UNICAMP), IFGW, Campinas, SP, Brazil*
[22]*Universidade Estadual de Feira de Santana, Feira de Santana, Brazil*
[23]*Universidade Federal do ABC, Santo André, SP, Brazil*
[24]*Universidade Federal do Paraná, Setor Palotina, Palotina, Brazil*
[25]*Universidade Federal do Rio de Janeiro, Instituto de Física, Rio de Janeiro, RJ, Brazil*
[26]*Universidad de Medellín, Medellín, Colombia*
[27]*Universidad Industrial de Santander, Bucaramanga, Colombia*
[28]*Charles University, Faculty of Mathematics and Physics, Institute of Particle and Nuclear Physics, Prague, Czech Republic*
[29]*Institute of Physics of the Czech Academy of Sciences, Prague, Czech Republic*
[30]*Palacky University, Olomouc, Czech Republic*
[31]*CNRS/IN2P3, IJCLab, Université Paris-Saclay, Orsay, France*
[32]*Laboratoire de Physique Nucléaire et de Hautes Energies (LPNHE), Sorbonne Université, Université de Paris, CNRS-IN2P3, Paris, France*
[33]*Université Paris-Saclay, CNRS/IN2P3, IJCLab, Orsay, France*
[34]*Bergische Universität Wuppertal, Department of Physics, Wuppertal, Germany*
[35]*Karlsruhe Institute of Technology (KIT), Institute for Experimental Particle Physics, Karlsruhe, Germany*
[36]*Karlsruhe Institute of Technology (KIT), Institut für Prozessdatenverarbeitung und Elektronik, Karlsruhe, Germany*
[37]*Karlsruhe Institute of Technology (KIT), Institute for Astroparticle Physics, Karlsruhe, Germany*
[38]*RWTH Aachen University, III. Physikalisches Institut A, Aachen, Germany*
[39]*TU Dortmund University, Department of Physics, Dortmund, Germany*
[40]*Universität Hamburg, II. Institut für Theoretische Physik, Hamburg, Germany*
[41]*Universität Siegen, Department Physik—Experimentelle Teilchenphysik, Siegen, Germany*
[42]*Gran Sasso Science Institute, L'Aquila, Italy*
[43]*INFN Laboratori Nazionali del Gran Sasso, Assergi (L'Aquila), Italy*
[44]*INFN, Sezione di Catania, Catania, Italy*
[45]*INFN, Sezione di Lecce, Lecce, Italy*
[46]*INFN, Sezione di Milano, Milano, Italy*
[47]*INFN, Sezione di Napoli, Napoli, Italy*

[48]*INFN, Sezione di Roma "Tor Vergata", Roma, Italy*
[49]*INFN, Sezione di Torino, Torino, Italy*
[50]*Osservatorio Astrofisico di Torino (INAF), Torino, Italy*
[51]*Politecnico di Milano, Dipartimento di Scienze e Tecnologie Aerospaziali, Milano, Italy*
[52]*Università del Salento, Dipartimento di Matematica e Fisica "E. De Giorgi", Lecce, Italy*
[53]*Università dell'Aquila, Dipartimento di Scienze Fisiche e Chimiche, L'Aquila, Italy*
[54]*Università di Catania, Dipartimento di Fisica e Astronomia "Ettore Majorana", Catania, Italy*
[55]*Università di Milano, Dipartimento di Fisica, Milano, Italy*
[56]*Università di Napoli "Federico II", Dipartimento di Fisica "Ettore Pancini", Napoli, Italy*
[57]*Università di Palermo, Dipartimento di Fisica e Chimica "E. Segrè", Palermo, Italy*
[58]*Università di Roma "Tor Vergata", Dipartimento di Fisica, Roma, Italy*
[59]*Università Torino, Dipartimento di Fisica, Torino, Italy*
[60]*Benemérita Universidad Autónoma de Puebla, Puebla, México*
[61]*Unidad Profesional Interdisciplinaria en Ingeniería y Tecnologías Avanzadas del Instituto Politécnico Nacional (UPIITA-IPN), México, D.F., México*
[62]*Universidad Autónoma de Chiapas, Tuxtla Gutiérrez, Chiapas, México*
[63]*Universidad Michoacana de San Nicolás de Hidalgo, Morelia, Michoacán, México*
[64]*Universidad Nacional Autónoma de México, México, D.F., México*
[65]*Institute of Nuclear Physics PAN, Krakow, Poland*
[66]*University of Łódź, Faculty of High-Energy Astrophysics,Łódź, Poland*
[67]*Laboratório de Instrumentação e Física Experimental de Partículas—LIP and Instituto Superior Técnico —IST, Universidade de Lisboa—UL, Lisboa, Portugal*
[68]*"Horia Hulubei" National Institute for Physics and Nuclear Engineering, Bucharest-Magurele, Romania*
[69]*Institute of Space Science, Bucharest-Magurele, Romania*
[70]*Center for Astrophysics and Cosmology (CAC), University of Nova Gorica, Nova Gorica, Slovenia*
[71]*Experimental Particle Physics Department, J. Stefan Institute, Ljubljana, Slovenia*
[72]*Universidad de Granada and C.A.F.P.E., Granada, Spain*
[73]*Instituto Galego de Física de Altas Enerxías (IGFAE), Universidade de Santiago de Compostela, Santiago de Compostela, Spain*
[74]*IMAPP, Radboud University Nijmegen, Nijmegen, The Netherlands*
[75]*Nationaal Instituut voor Kernfysica en Hoge Energie Fysica (NIKHEF), Science Park, Amsterdam, The Netherlands*
[76]*Stichting Astronomisch Onderzoek in Nederland (ASTRON), Dwingeloo, The Netherlands*
[77]*Case Western Reserve University, Cleveland, Ohio, USA*
[78]*Colorado School of Mines, Golden, Colorado, USA*
[79]*Department of Physics and Astronomy, Lehman College, City University of New York, Bronx, New York, USA*
[80]*Michigan Technological University, Houghton, Michigan, USA*
[81]*New York University, New York, New York, USA*
[82]*University of Chicago, Enrico Fermi Institute, Chicago, Illinois, USA*
[83]*University of Delaware, Department of Physics and Astronomy, Bartol Research Institute, Newark, Delaware, USA*

(Received 14 May 2026; accepted 9 July 2026; published 10 August 2026)

We present measurements of the depth of shower maximum, $X_{\max}$, for cosmic-ray-induced extensive air showers recorded by the fluorescence detector of the Pierre Auger Observatory over 17 years. The dataset covers primary energies from $10^{17.7}$ eV to beyond $10^{19.6}$ eV. With improved event reconstruction and an

[a]Max-Planck-Institut für Radioastronomie, Bonn, Germany.
[b]also at Kapteyn Institute, University of Groningen, Groningen, The Netherlands.
[c]School of Physics and Astronomy, University of Leeds, Leeds, United Kingdom.
[d]Fermi National Accelerator Laboratory, Fermilab, Batavia, Illinois, USA (Affiliation for identification purposes only).
[e]Pennsylvania State University, University Park, Pennsylvania , USA.
[f]Colorado State University, Fort Collins, Colorado, USA.
[g]Louisiana State University, Baton Rouge, Louisiana, USA.
[h]Université Grenoble Alpes, CNRS, Grenoble Institute of Engineering, LPSC-IN2P3, Grenoble, France.
[i]now at Graduate School of Science, Osaka Metropolitan University, Osaka, Japan.
[j]Institut universitaire de France (IUF), France.

Published by the American Physical Society under the terms of the Creative Commons Attribution 4.0 International license. Further distribution of this work must maintain attribution to the author(s) and the published article's title, journal citation, and DOI.

exposure 2.4 times larger than in our previous analysis, this work confirms and refines our conclusions on the mass composition at ultrahigh energies. The energy evolution of the mean $X_{\max}$ exhibits a pronounced break at a cosmic-ray energy of about $10^{18.4}$ eV, providing direct, model-independent evidence for a change in the evolution of the mass composition. Independently, the observed decrease of the $X_{\max}$ fluctuations with energy indicates a transition toward a heavier and less diverse primary mass composition. No statistically significant declination dependence of the $X_{\max}$ distributions is observed within the exposure of the Observatory, consistent with an isotropic mass composition at the sensitivity of this analysis. The mean and standard deviation of the $X_{\max}$ distributions, interpreted with air-shower simulations, yield the energy dependence of the average and variance of the logarithmic mass of cosmic rays arriving at Earth. Furthermore, energy-dependent fractional abundances of four representative primary-mass groups (p, He, CNO, Fe) are obtained by fitting the observed $X_{\max}$ distributions in each energy bin with a weighted sum of elemental templates. These results provide strong evidence against a long-standing assumption that ultrahigh-energy cosmic rays are predominantly protons: above $\sim 10^{18.4}$ eV, the average cosmic-ray mass increases, accompanied by a steadily decreasing diversity in the elemental composition.

DOI: 10.1103/n616-15v5

I. INTRODUCTION

The elemental composition of ultrahigh-energy cosmic rays (UHECRs) is a fundamental observable for understanding their origin, providing key insights into the astrophysical sources and acceleration mechanisms that produce these rare, energetic particles (see, e.g., Ref. [1] for a recent review). However, determining the mass composition of UHECRs is challenging. When a primary cosmic-ray particle enters the atmosphere, it interacts with air nuclei and initiates an extensive air shower. The longitudinal particle profile of an air shower peaks once the cascade reaches a certain slant depth, at which the average electromagnetic energy is so low that most energy is lost through ionization rather than through the production of new particles. This depth of shower maximum, $X_{\max}$, is correlated with the mass of the primary cosmic ray [2–7]. However, reconstructing the mass of individual events from $X_{\max}$ alone is impossible because of large event-to-event fluctuations in the shower development. Moreover, despite substantial progress in modeling hadronic interactions at ultrahigh energies [8–12], air-shower physics at energies beyond terrestrial accelerators still carries significant and difficult-to-quantify systematic uncertainties, see, e.g., Ref. [13].

Experimentally, these particle cascades can be investigated using two complementary detection methods: ground-based surface detectors, which sample the secondary particles that reach the Earth's surface, and fluorescence telescopes, which record the ultraviolet light emitted when atmospheric nitrogen molecules return to their ground state after being excited by secondary particles. Thus, fluorescence telescopes can directly observe the atmospheric development of air showers, providing a unique advantage for mass-composition studies, despite the limited duty cycle of $\sim$15% for ground-based instruments during clear, moonless nights.

In this paper, we present a detailed analysis of the distributions of the depth of shower maximum ($X_{\max}$), recorded by the fluorescence telescopes of the Pierre Auger Observatory [14]. This study expands upon our previous mass-composition analyses with the fluorescence detector of the Observatory [15–17], incorporating improved event reconstruction methods and utilizing the full dataset collected from 2004 to 2021, prior to the AugerPrime surface-detector upgrade [18].

The paper is structured as follows. Section II briefly describes the Pierre Auger Observatory. The data analysis and event selection are described in Sec. III, while detector effects including acceptance, resolution, reconstruction bias, and the systematic uncertainty on the $X_{\max}$ scale are characterized in Sec. IV. The robustness of the analysis is assessed in Sec. V through a series of validation studies. Measurements of the $X_{\max}$ moments and their interpretation in terms of the moments of logarithmic cosmic-ray mass are presented in Sec. VI. Finally, the $X_{\max}$ distributions are fitted in Sec. VII to extract the energy-dependent fractional composition of cosmic-ray primaries, and Sec. VIII summarizes the results.

II. THE PIERRE AUGER OBSERVATORY

The Pierre Auger Observatory, the largest cosmic-ray observatory ever built, spans an area of 3000 km^2 near Malargüe, Argentina, at an average altitude of 1400 meters above sea level [14]. This paper focuses on the data collected using the Surface Detector (SD) [19] and Fluorescence Detector (FD) [20] of the Observatory in their baseline configuration [21]. In this configuration, the SD comprises 1600 water-Cherenkov stations arranged in a triangular grid with 1500 m spacing. The FD consists of 24 fluorescence telescopes installed in groups of six at four sites around the SD, with an elevation coverage from 1.5° to 30°. The data collected using low-energy enhancements, namely the SD region with a 750 m grid size [22] and the

high-elevation telescopes with an elevation range from 30° to 58° [23], will be utilized in a future paper to extend $X_{\max}$ measurements down to an energy of about $10^{17.2}$ eV.

To ensure a high-quality reconstruction of the shower energy and $X_{\max}$, a reliable calibration of the fluorescence telescopes and a solid knowledge of atmospheric conditions at the time of observation are necessary. An absolute calibration and nightly relative calibrations are required to estimate the number of photons at the aperture of the telescope from the ADC counts recorded by the PMTs. The absolute calibration is performed using a Lambertian light source of known intensity, while LEDs mounted on the mirrors are for the nightly relative calibration [24–26]. The Global Data Assimilation System (GDAS) provides atmospheric molecular density profiles on a 3-hour basis [27]. The aerosol content of the atmosphere is monitored constantly during observations via vertical laser shots from which the density profiles of aerosols above the array are derived for each fluorescence telescope site on an hourly basis [28,29]. Here we use the recently improved aerosol determination described in Ref. [30]. Finally, clouds are monitored both using an infrared camera at each FD site [31] and from the Geostationary Operational Environmental Satellites (GOES) [32].

The ground-level impact point and arrival direction of each event are reconstructed using a hybrid method [33,34], combining the classical FD geometry fit [35] with the position and time of particles recorded in the SD station nearest to the shower axis, yielding substantially improved geometric reconstruction [34]. The calorimetric energy [36] and the depth of shower maximum are determined in a likelihood fit, based on Ref. [37], to the photoelectrons detected by the FD telescopes. A Gaisser-Hillas function [38] is used to describe the longitudinal energy-deposit profile. We employ the modified representation of the Gaisser-Hillas function [39], which allows for improved constraints on the shape parameters of the longitudinal profile, as discussed in Ref. [40]. From this profile, we compute the expected fluorescence and Cherenkov light, propagate it through the atmosphere, and fold it with the optical response of the telescopes to obtain the predicted photoelectrons which are compared with the measurements.

The total energy of the shower is obtained by correcting the calorimetric energy for the fraction carried away by neutrinos and high-energy muons, following Ref. [41]. Throughout this paper, we use the total energy of the primary particle. The combined uncertainties from calibration, atmospheric monitoring, and event reconstruction contribute to a systematic uncertainty of 14% on the energy determination [42].

III. DATA SELECTION

The dataset includes events recorded using the FD and SD between December 1, 2004, and December 31, 2021.

TABLE I. Selection criteria, number of events passing the selection, and efficiency ε with respect to the previous step. The last row reports the number of unique air showers obtained after merging high-quality FD stereo events.

	Events	ε/%
Air-shower candidates	5,311,333	⋯
Preselection:		
Hardware status	4,283,450	80.6
Aerosols	3,479,008	81.2
Hybrid geometry	1,249,849	35.9
Profile reconstruction	1,038,782	83.1
Clouds	769,699	74.1
$E \geq 10^{17.7}$ eV	281,562	36.6
Quality and fiducial selection:		
P(hybrid)	277,378	98.5
$X_{\max}$ observed	218,904	78.9
Quality	156,015	71.3
Fiducial field of view	60,189	38.6
Profile	58,887	97.8
Unique air-shower events	58,453	

The event selection and analysis are based on our previous publication [16], which provides more comprehensive details on all key steps. The dataset contains 5,311,333 air-shower candidates, from which we select 58,453 high-quality air-shower events using the cuts listed in Table I and described below.

A. Preselection

The first stage of the pre-selection focuses on the hardware status of the FD telescopes. Candidate events are retained only for time periods in which the telescope optics are properly aligned, the PMT gains of the cameras are well calibrated, and the FD-SD timing is sufficiently synchronized to allow an accurate hybrid reconstruction. These conditions are verified using the electronic logs and slow-control data associated with each event.

Next, the atmospheric conditions are assessed, since poor atmospheric quality can introduce significant uncertainties in the correction for fluorescence-light attenuation. If no aerosol measurement from the laser facilities is available within one hour of the event time, the candidate is rejected. Otherwise, the vertical aerosol optical depth (VAOD), integrated from ground level up to 3 km altitude, must be below 0.1, ensuring a vertical transmission of about 90%. Higher VAOD values lead to substantial and difficult-to-correct attenuation of the fluorescence light [29].

An event is retained only if at least one SD station is triggered within the timing and geometric window consistent with the FD observation, ensuring that a hybrid geometry reconstruction is possible. Events rejected by this criterion are typically low-energy showers with insufficient

ground-level particle density to trigger the SD-1500 array [43], or meteorological events that satisfy the FD trigger but cannot be reconstructed. A successful reconstruction of the longitudinal energy-deposit profile is also required.

To exclude air showers for which the light may be obscured or reflected by clouds, cloud coverage is monitored using the devices described in Sec. II. Events are retained if no clouds are detected in the shower direction in either the telescope projection (cloud infrared camera) or the ground-level projection (GOES), or if the average cloud fraction measured by the LIDARs is below 25% [44].

Finally, the analysis is restricted to events with energies above $10^{17.7}$ eV. Below this threshold, the enlarged field of view of the high-elevation telescopes is needed, which will be addressed in a separate paper.

After this preselection, 281,562 air-shower events remain for further analysis.

B. Quality selection

The next selection cut aims to reduce a possible bias arising from the different probabilities for a single-station SD trigger in proton- and iron-induced air showers. The single-station probability quantifies the probability that an SD station at the corresponding core distance would satisfy the local trigger condition for a shower with the given energy and zenith angle. For each event, this probability is estimated from its energy, zenith angle, and core location using the data-driven lateral trigger probability described in Ref. [43]. Requiring it to exceed 95% selects events for which the SD trigger is nearly fully efficient, thereby reducing composition-dependent trigger biases.

Furthermore, we accept only events whose longitudinal profiles include the shower maximum within the field of view of the telescopes, since $X_{\max}$ cannot be reliably determined when only the rising or falling edge of the profile is observed.

The next step removes events with large expected uncertainties in the $X_{\max}$ reconstruction. The expected uncertainty, $\hat{\sigma}$, is computed from the event energy and geometry, and only events with $\hat{\sigma} \leq 40$ g cm^{-2} are retained. In addition, showers for which the minimum observation angle, $\alpha_{\min}$, with respect to the shower axis is smaller than 20° are discarded. The significant contribution of direct Cherenkov light and the short time duration of the detected light at such small viewing angles can lead to substantial $X_{\max}$ biases.

After the fiducial cuts described below in Sec. III C are applied, an additional final set of quality cuts is applied to the reconstructed energy-deposit profile to ensure an accurate determination of $X_{\max}$ and energy. The minimum observed profile length must exceed 200 g cm^{-2}, and any gaps within the profile, such as those arising in telescope-crossing showers, must constitute less than 20% of the total profile length. Profiles distorted by residual cloud or aerosol contamination cannot be fitted reliably. To remove such cases, we evaluate the goodness of the Gaisser-Hillas profile fit using the transformed statistic $z = (\chi^2 - \mathrm{ndf})/\sqrt{2\mathrm{ndf}}$. The central part of the observed distribution is approximately Gaussian, while a non-Gaussian tail appears at large positive values. We exclude events at the onset of this tail, corresponding to about 2.7 standard deviations above the center of the approximately Gaussian part of the distribution. This cut differs from that used in our previous analysis [16] because of the change in the Gaisser-Hillas parametrization described in Ref. [40].

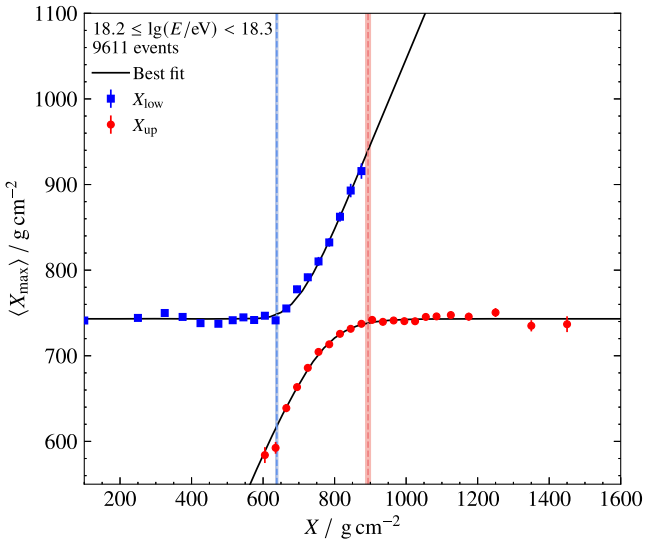


FIG. 1. Determination of the fiducial field-of-view limits $(X^{\rm fid}_{\rm low}, X^{\rm fid}_{\rm up})$, marked by the vertical lines, for the energy bin $18.2 \leq \lg(E/\mathrm{eV}) < 18.3$. Their widths indicate the uncertainties on the corresponding fiducial limits. Data points show the truncated mean of the $X_{\max}$ distribution above $X_{\rm low}$ and below $X_{\rm up}$.

C. Fiducial selection

With the selection described so far, the dataset contains only events with a high-quality reconstruction. However, this is not sufficient to avoid selection effects. As discussed in Ref. [16], which also provides a geometrical illustration, the field of view of the FD telescopes introduces a selection bias that depends on the shower $X_{\max}$, core position, arrival direction, and energy. To minimize this bias, a slant-depth interval $(X_{\rm low}, X_{\rm up})$ is calculated for each event such that any $X_{\max}$ lying within that interval would satisfy the dominant $X_{\max}$ quality requirements, $\hat{\sigma} < 40$ g cm^{-2} and $\alpha_{\min} > 20°$. An event is accepted only if its $(X_{\rm low}, X_{\rm up})$ interval is sufficiently large to accommodate the bulk of the $X_{\max}$ distribution in the data [16].

Since the true $X_{\max}$ distribution is not known at this stage, the fiducial field-of-view boundaries are determined by studying the bias on $\langle X_{\max}\rangle$ as a function of $(X_{\rm low}, X_{\rm up})$ for each energy bin, an example of which is shown in Fig. 1. Once the field of view begins truncating the $X_{\max}$ distribution, the observed $\langle X_{\max}\rangle$ deviates from its unbiased

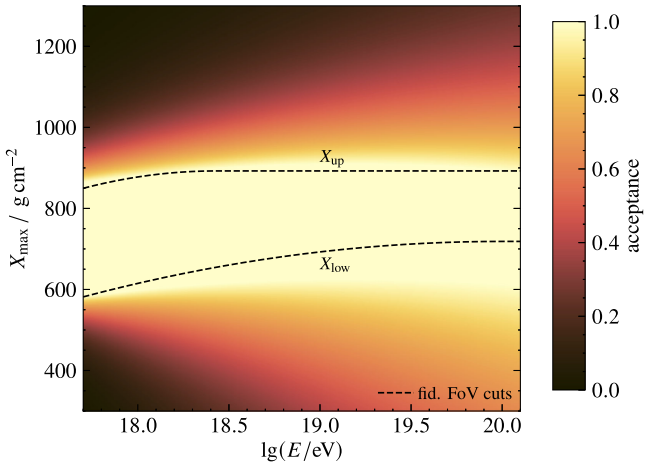


FIG. 2. Fiducial field-of-view boundaries from Eq. (1) (black dashed lines) and $X_{\rm max}$ acceptance as defined in Sec. IV A (color scale) as a function of $X_{\rm max}$ and energy.

asymptotic value. The fiducial field-of-view boundaries, indicated by the vertical lines in Fig. 1, correspond to a $\langle X_{\rm max}\rangle$ bias of 5 g cm^{-2}. The energy dependence of these boundaries is parametrized as

$$X^{\rm fid}_{\rm up/low}(E) = \begin{cases} X_0 + K \lg^2(E/E_0) & \text{if } E \le E_0, \\ X_0 & \text{otherwise.} \end{cases} \quad (1)$$

The fit of (X_0, K, lg E_0) yields values of (892.51, −80.39, 18.43) for $X^{\rm fid}_{\rm up}$ and (718.56, −25.88, 20.00) for $X^{\rm fid}_{\rm low}$, where X_0 and K are given in units of g cm^{-2}, and E_0 in eV. An event of energy E is retained if $X_{\rm low} < X^{\rm fid}_{\rm low}(E)$ and $X_{\rm up} > X^{\rm fid}_{\rm up}(E)$. The behavior of the field-of-view boundaries as a function of energy is shown by the black dashed lines in Fig. 2.

D. Final dataset

After this rigorous selection process, 58,887 events from individual FD sites remain in the final dataset, corresponding to about 1% of the initial air-shower candidates. Events observed by more than one FD site are merged by calculating uncertainty-weighted averages of their $X_{\rm max}$ and energy. This procedure yields a final high-quality dataset of 58,453 unique air-shower events. The $X_{\rm max}$ and energy distributions of these events are shown in Fig. 3. For illustration, the $\langle X_{\rm max}\rangle$ and $\sigma(X_{\rm max})$ values computed later in this paper are also displayed. The distribution of $X_{\rm max}$ in energy bins of 0.1 in lg(E/eV) are displayed in Fig. 4. The last energy range contains all events above $10^{19.6}$ eV. The energy of the highest-energy event is $(1.17 \pm 0.07(\text{stat})) \times 10^{20}$ eV and its $X_{\rm max}$ is $817 \pm 25(\text{stat})$ g cm^{-2}, where the quoted uncertainties are statistical.

A list of all selected events is available from Ref. [45].

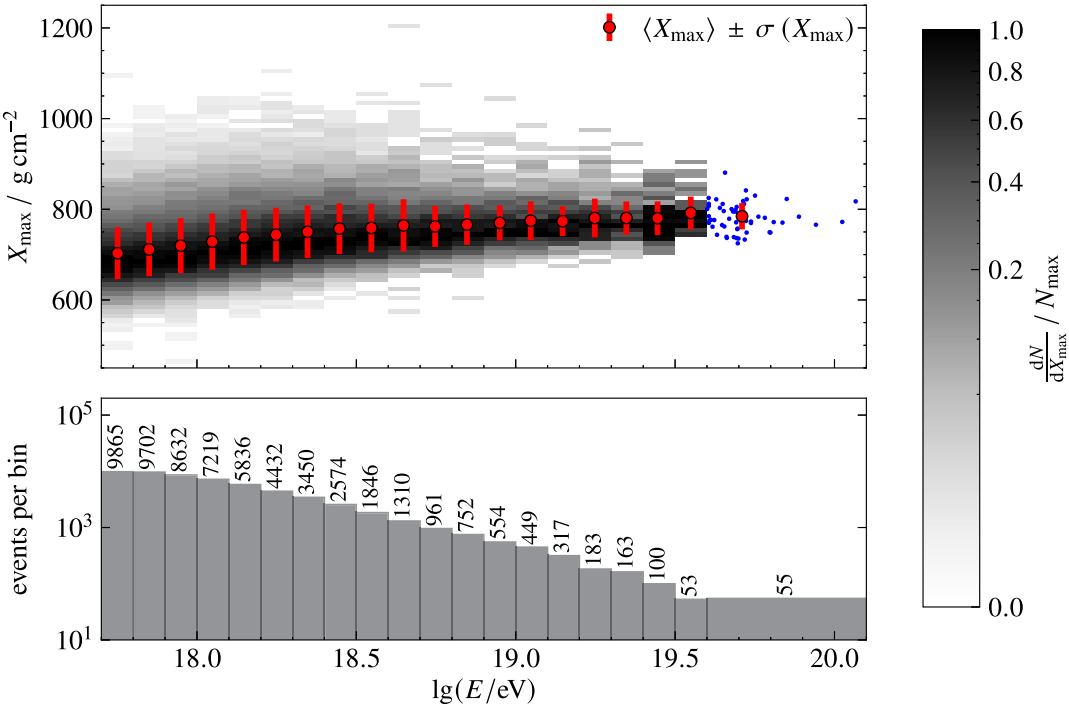


FIG. 3. Top panel: Measured $X_{\rm max}$ and energy of the events selected for this analysis. The event density is shown in grayscale, normalized to the entries of the maximum bin at each energy. Individual events above $10^{19.6}$ eV are displayed as blue points. The large red points represent the mean of the $X_{\rm max}$ distribution in each energy bin, and the error bars indicate its standard deviation. Bottom panel: Number of selected events as a function of energy.

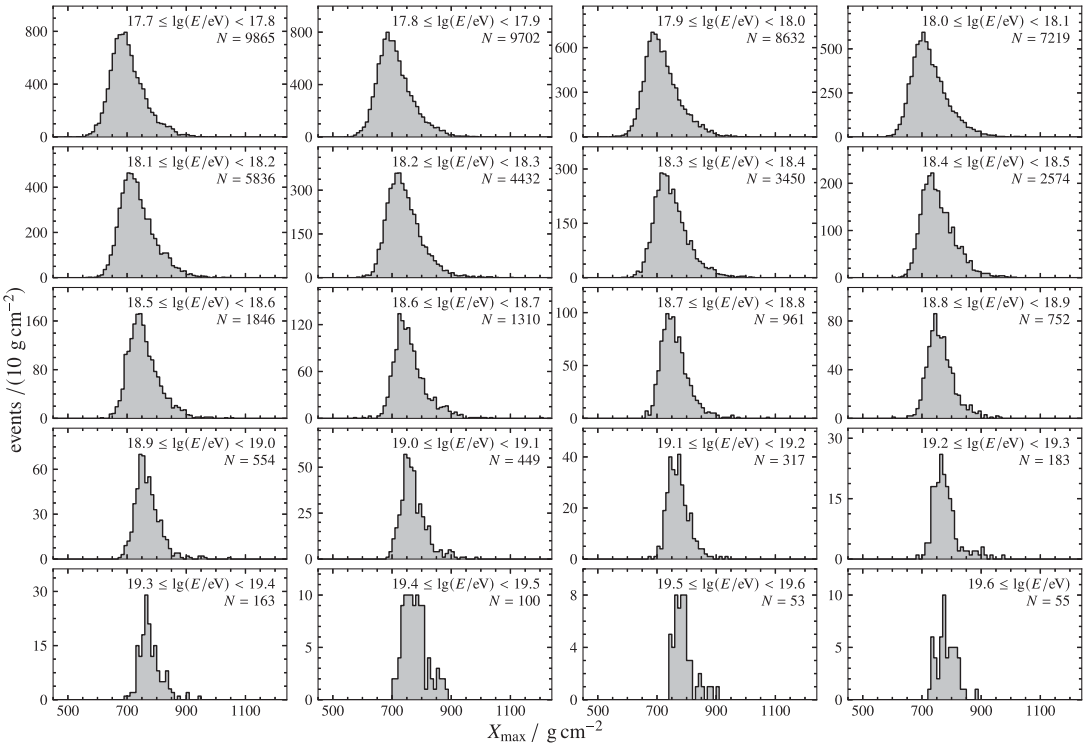


FIG. 4. $X_{\max}$ distributions in different energy bins.

IV. DETECTOR EFFECTS AND SYSTEMATICS

The $X_{\max}$ distributions shown in Fig. 4 differ from the true distributions of air showers in the atmosphere due to residual sampling and reconstruction biases, and the finite $X_{\max}$ resolution. The quality and fiducial selection have been designed to keep these distortions small, but they are not negligible for a precise determination of the moments of the distribution or for a fit with composition templates. In the following, we characterize these measurement effects.

The relation between the true and observed $X_{\max}$ distributions, $f(X_{\max})$ and $f_{\rm obs}(X_{\max}{}^{\rm rec})$ respectively, is given by the convolution,

$$f_{\rm obs}(X^{\rm rec}_{\max}) = \int_0^\infty f(X_{\max}) R(X^{\rm rec}_{\max} - X_{\max} + \Delta) \times \varepsilon(X_{\max}) {\rm d}X_{\max}, \quad (2)$$

where $\varepsilon(X_{\max})$ is the probability of observing and selecting an event with a given shower maximum, denoted as "acceptance", and $R(X^{\rm rec}_{\max} - X_{\max})$ is the detector response, including resolution and bias. Δ denotes a systematic shift in the $X_{\max}$ scale that is usually unknown, but whose plausible range, commonly referred to as the *systematic uncertainty*, can be estimated.

The acceptance and resolution are evaluated using detailed simulations that replicate the time-dependent state of the SD, FD, and atmosphere [46,47]. Longitudinal air-shower profiles are generated with the CONEX program [48] using SIBYLL 2.3d [10] and URQMD1.3 [49] for high- and low-energy hadronic interactions, respectively. The detector simulation and event reconstruction are carried out using the Offline framework of the Pierre Auger Observatory [50]. The simulated showers are reconstructed and selected in the same manner as the measurements.

The acceptance and resolution derived from the simulation are to good approximation independent of the choice of hadronic interaction model or mass composition, because longitudinal air shower profiles are universal for a given $X_{\max}$ and energy [39,51]. To achieve model independence, it is therefore sufficient to weight the simulated events such that the generated energy spectrum follows the measured one [42] and the $X_{\max}$ distribution of the simulated sample reproduces the observed one.

A. Acceptance

The acceptance is defined as the ratio of the number of selected events to the number of generated events as a function of $X_{\max}$. To obtain the *relative* acceptance at a particular energy, we normalize the acceptance to its maximum value. The resulting relative acceptance can be well-parametrized by a constant with exponentially rising and falling edges,

$$\varepsilon(X_{\max}) = \begin{cases} {\rm e}^{+(X_{\max}-X_1)/\lambda_1}, & X_{\max} < X_1; \\ 1, & X_1 \le X_{\max} \le X_2; \\ {\rm e}^{-(X_{\max}-X_2)/\lambda_2}, & X_2 < X_{\max}. \end{cases} \quad (3)$$

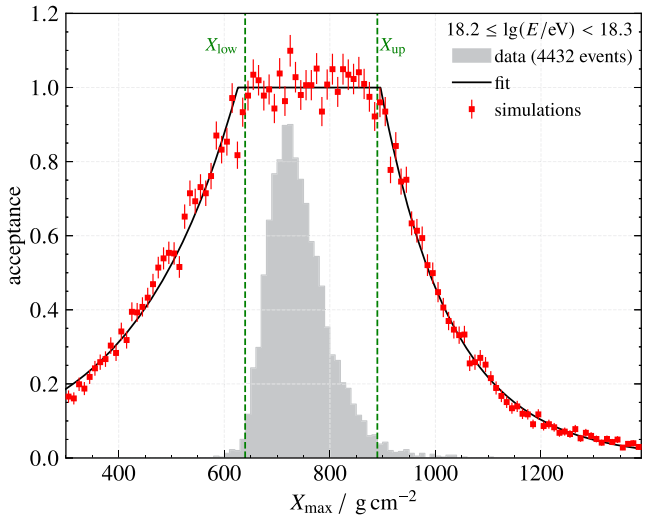


FIG. 5. Acceptance as a function of X_{max} in simulations (points) in the energy interval $18.2 \leq \lg(E/\mathrm{eV}) < 18.3$. The fit with Eq. (3) is shown as a dashed line. For comparison, the distribution of X_{max} of the data in this energy range is shown as a gray histogram (arbitrary normalization).

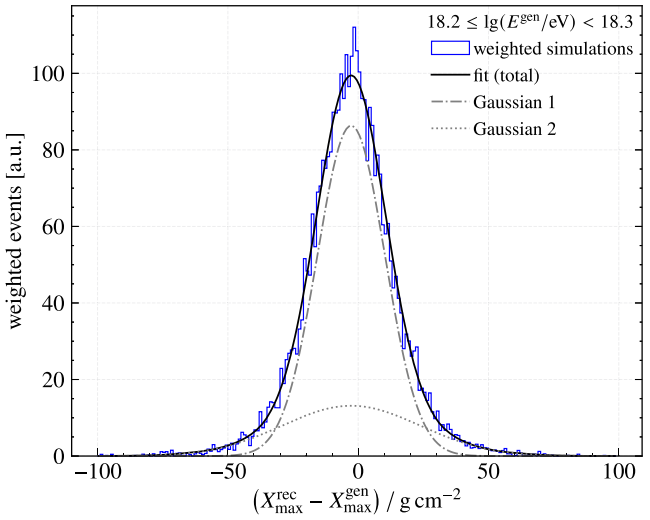


FIG. 6. Distribution of the difference between reconstructed and generated X_{max} for simulated showers in the energy interval $18.2 \leq \lg(E/\mathrm{eV}) < 18.3$. The events are weighted to match the X_{max} distribution in the data. The fit with Eq. (4) is shown with a blue dashed line, while the broad and narrow Gaussians that compose it are represented with dotted and dash-dotted lines, respectively.

The parameters $(X_1, X_2, \lambda_1, \lambda_2)$ are energy-dependent as specified in Appendix B 1. An example of the acceptance using simulations in the energy interval $18.2 \leq \lg(E/\mathrm{eV}) < 18.3$, fitted with Eq. (3), is presented in Fig. 5 along with the X_{max} distribution in the data. By construction, most of the observed events fall within the fiducial X_{max} range, $(X^{fid}_{low}, X^{fid}_{up})$, displayed by vertical dashed lines. Within this slant depth range, the acceptance is found to be constant, demonstrating the desired effect of the fiducial-field-of-view selection to ensure an equal-probability sampling of air showers with a shower maximum within this range. The energy dependence of the acceptance is displayed in Fig. 2. As can be seen, the fiducial X_{max} range is well contained in the flat part of the acceptance, i.e., $X_1 \leq X^{fid}_{low}$ and $X^{fid}_{up} \leq X_2$.

B. X_{max} bias and resolution

1. Detector response from simulations

The detector response $R(X^{rec}_{max} - X_{max})$ of the reconstructed X^{rec}_{max} of simulated showers after detector simulation can be well described empirically by the sum of two Gaussian distributions, G,

$$R(X^{rec}_{max} - X_{max}) = fG(\mu, \sigma_1) + (1-f)G(\mu, \sigma_2). \quad (4)$$

This double-Gaussian parametrization provides an empirical approximation of the detector response obtained after averaging over showers with different geometries, for which the X_{max} resolution varies, and thereby describes the resulting non-Gaussian shape. Here f denotes the relative contribution of the first Gaussian, and $\sigma_1 < \sigma_2$, the widths of the first and second Gaussians, respectively. The mean of R is the X_{max} reconstruction bias μ_R and its standard deviation $(f\sigma_1^2 + (1-f)\sigma_2^2)^{\frac{1}{2}}$ is the X_{max} resolution. The resolution quantifies the broadening of the X_{max} distribution and the bias of its offset.

The fitted parameters of R depend slightly on X_{max} [52], but for the purpose of this analysis we use an effective response averaged over the X_{max} distribution. This is obtained by weighting the simulated showers to match the observed X_{max} distribution.

In Fig. 6, an example of R in the energy interval $18.2 \leq \lg(E/\mathrm{eV}) < 18.3$ is shown, along with a fit to Eq. (4). Most of the detector response is described by the narrow Gaussian with width σ_1, whereas the broad Gaussian with width σ_2 describes the tails of the response.

The energy evolution of the X_{max} bias is shown in Fig. 7. The fitted μ_R value is shown with blue points, and its parametrization, $\mu_R/(\mathrm{g\,cm^{-2}}) = -2.9 + 0.4\ \lg(E/\mathrm{EeV})$, is shown as a blue line. It varies from approximately -3 g cm^{-2} at the lowest energies to -2 g cm^{-2} at 10^{20} eV. We correct each event for this average bias by subtracting $\mu_R(E)$ from the reconstructed X_{max}.

The resolution derived from simulation captures the statistical fluctuations of the reconstructed X_{max} due to the finite number of photoelectrons detected by the photomultipliers of the fluorescence telescopes. It therefore includes contributions from the uncertainty in the shower geometry and from the fit to the longitudinal profile. It decreases from $\sim$25 g cm^{-2} at $10^{17.6}$ eV to $\sim$12 g cm^{-2} at $10^{19.0}$ eV.

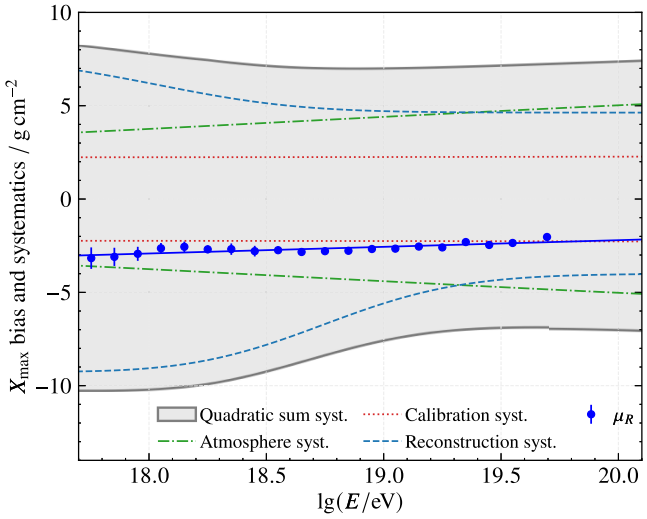


FIG. 7. Reconstruction bias (points) and systematic uncertainties in the X_{max} scale from the detector calibration, reconstruction, and atmosphere (lines) as a function of energy.

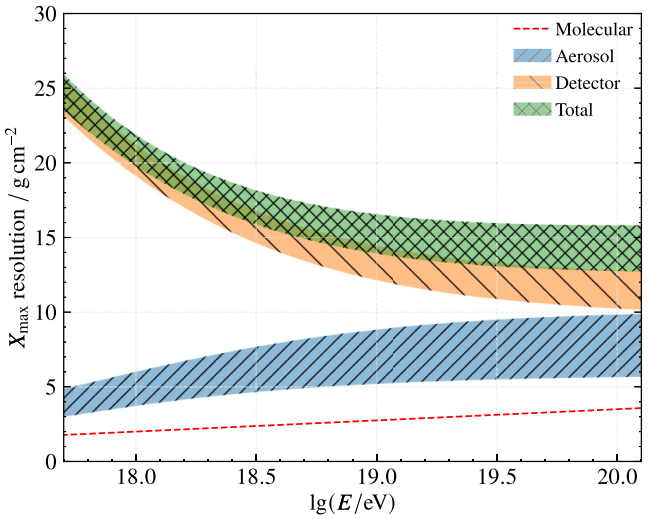


FIG. 8. The total X_{max} resolution and the individual contributions from detector, aerosols, and density profiles as a function of energy. Shaded bands indicate the systematic uncertainties.

2. Additional contributions to the X_{max} resolution

The detector response is further broadened by the following contributions that are not included in the simulations:

a. Telescope alignment This analysis utilizes data recorded by 24 individual fluorescence telescopes. The angular alignment of each telescope was determined using two methods; observations of UV star tracks and using the independent reconstruction of the shower geometry available for high-quality SD events. The reconstruction of the data with either set of alignment constants yields no difference in X_{max} on average, but the standard deviation of the distribution of X_{max} differences between the two reconstructions can be used as an estimate of the possible influence of the telescope-alignment uncertainty on the X_{max} resolution. We find a standard deviation of $\delta = (5.07 + 0.87\lg(E/10^{17.55}\ \text{eV}))\ \text{g cm}^{-2}$. We take $\delta/2$ as an estimate of the alignment contribution to the X_{max} resolution with a systematic uncertainty of $\pm\delta/2$.

b. Aerosols The statistical uncertainty of the measurements of aerosols constitutes an additional contribution to the overall X_{max} resolution. This uncertainty originates from fluctuations in the night-sky background, the number of photons detected from laser shots, and the variability of aerosol content relative to the hourly average values. It is estimated from the standard deviation of quarter-hourly VAOD measurements [53]. A second contribution arises from the nonuniformity of the aerosol layers over the array. It is assessed using observations from different FD sites [29].

c. Molecular atmosphere Another contribution arises from the uncertainty in the atmospheric density profile at the time of an event. It is evaluated by comparing X_{max} values reconstructed using GDAS with those obtained from balloon soundings available for a fraction of the data [27].

3. Full X_{max} resolution

The additional contributions are assumed to be Gaussian, and their widths are added in quadrature to the double-Gaussian parametrization obtained from simulations. The resulting parameters are listed in Appendix B 2.

The standard deviation of the full X_{max} response function is shown in Fig. 8. It improves from 25 g cm^{-2} at $10^{17.7}$ eV to 16 g cm^{-2} at $10^{19.0}$ eV, remaining approximately constant at higher energies. The quadratic sum of the statistical resolution (derived from simulations) and the telescope alignment is shown in Fig. 8 with an orange band. The decrease of this contribution with energy is mainly due to the increased brightness of air showers at higher energies and due to the larger fraction of events observed at more than one FD site. The contribution from aerosols, shown with a blue band, increases with energy, as high-energy showers can be viewed at larger distances and, correspondingly, the correction for aerosol transmission increases. The uncertainty of the molecular atmosphere is shown as a dashed red line and remains below 4 g cm^{-2} at all energies.

C. X_{max} scale uncertainty

The estimated systematic uncertainty on the X_{max} scale Δ in Eq. (2) is displayed in Fig. 7. It changes from $^{+8.1}_{-10.2}$ g cm^{-2} at $10^{17.7}$ eV to about ± 7 g cm^{-2} at 10^{20} eV and is attributed to three main contributions discussed in the following.

a. Detector calibration The uncertainty associated with the relative timing between the FD and SD is estimated to be $\pm 2\text{g/cm}^2$ from dedicated reconstructions with a systematic shift of ± 100 ns applied to the relative timing constants. The calibration of the relative PMT responses adds an additional uncertainty of less than $\pm 1\text{g/cm}^2$, as

estimated from comparisons of data reconstructed with different versions of the calibration database.

b. Reconstruction Part of the uncertainty arising from shower-profile fitting is determined by varying the constraints of the shape parameters of the Gaisser-Hillas function within one standard deviation of their central values [40]. This contribution is $^{+4.6}_{-4.0}$ g cm^{-2} and remains constant with energy.

Additionally, an incomplete understanding of the interplay between the telescope point-spread function and the lateral distribution of the Cherenkov and fluorescence light leads to an energy-dependent $X_{\max}$ uncertainty. In the data, we find a larger fraction of light outside the collection angle than expected from simulations of the optical system and lateral light distribution from air showers. This mismatch depends on shower age, and its origin is not fully understood. The corresponding contribution to the $X_{\max}$ systematic uncertainty is found to be $^{+5.1}_{-8.3}$ g cm^{-2} at $10^{17.7}$ eV, decreasing to $^{+0.1}_{-0.6}$ g cm^{-2} at 10^{20} eV. The total reconstruction uncertainty amounts to $^{+6.9}_{-9.2}$ g cm^{-2} at $10^{17.7}$ eV and $^{+4.6}_{-4.0}$ g cm^{-2} at 10^{20} eV.

c. Atmosphere The 4% uncertainty in the absolute yield of the fluorescence light production [54] introduces an energy-independent $X_{\max}$ uncertainty of ± 0.4 g cm^{-2}. An additional contribution of ± 0.2 g cm^{-2} arises from the uncertainty in the wavelength dependence of fluorescence yield. Different parametrizations of multiple scattering of fluorescence light introduce another uncertainty of ± 2 g cm^{-2} [55]. At the highest energies, where showers can be observed at greater distances from the FD telescopes, the dominant contribution to atmospheric uncertainties arises from measurements of the aerosol content [29,53]. Recently, stereo observations of air showers [30] were used to cross-check and correct the VAOD impact on $X_{\max}$ and energy measurements. Overall, the VAOD contribution to the $X_{\max}$ systematic uncertainty amounts to ± 2.9 g cm^{-2} at $10^{17.7}$ eV and ± 4.6 g cm^{-2} at 10^{20} eV. The total uncertainty due to atmospheric effects increases with energy from ± 3.6 g cm^{-2} to ± 5.0 g cm^{-2}.

V. CROSS-CHECKS AND COMPARISONS OF DATA-SUBSETS

The systematic uncertainties discussed in the previous section have been thoroughly validated through extensive cross-checks of the stability of the results under detector, geometric, and atmospheric variations, and through tests of data-simulation consistency. The most relevant studies are summarized below.

A. Detector resolution

Events reconstructed by multiple FD sites can be used to validate the detector resolution obtained from simulation in Sec. IV. The distributions of the differences between the reconstructed $X_{\max}$ values at each participating site, $\Delta X_{\max}$, for data and simulation are shown in Fig. 9. The two distributions agree statistically, with a Baker-Cousins $\chi^2/\mathrm{ndf} = 26.1/23$ [56], indicating that the $X_{\max}$ resolution estimated from simulations is reliable. Two events with $\Delta X_{\max} \geq 100$ g cm^{-2} appear as outliers. Such events occur at a rate of 0.45% in the stereo dataset, which is statistically compatible with the rate of 0.20% found in simulations.

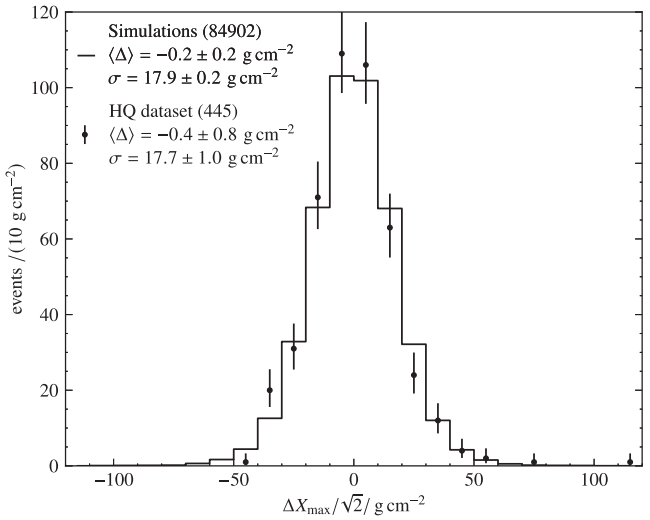


FIG. 9. Distribution of $X_{\max}$ difference for events observed at more than one FD site for data and simulation.

B. Analysis of simulated data

The analysis method can be validated end-to-end using simulations by comparing the reconstructed moments to the true moments at the generator level. The profiles of air showers induced by protons as well as helium, nitrogen, and iron nuclei are simulated with CONEX using the hadronic model SIBYLL 2.3d. As in Sec. IV, the simulations replicate the time-dependent state of the SD, FD, and atmosphere and are subjected to the same selection described in Sec. III.

Three checks are performed; one against each of the four simulated primary species, one against a 50/50 proton-iron mixture, and one against the fractional mix presented below in Sec. VII (the "Auger mix"), which closely follows the behavior of the measurements. Primary-specific acceptance and resolution are computed and used for the tests against single-element injection. For the mixed-composition tests, we use the acceptance and resolution from Sec. IV, since the corresponding simulations, by construction, closely reproduce the measured distributions.

Results for $\langle X_{\max} \rangle$ and $\sigma(X_{\max})$ are shown in Fig. 10. The points show the reconstructed values, and the lines show the generated ones. The difference Δ between reconstructed and generated values is shown in the lower panel of each figure, with the systematic uncertainty in the reconstruction shown in gray. Deviations are generally of order 2 to 5 g cm^{-2} for all compositions. These discrepancies stem

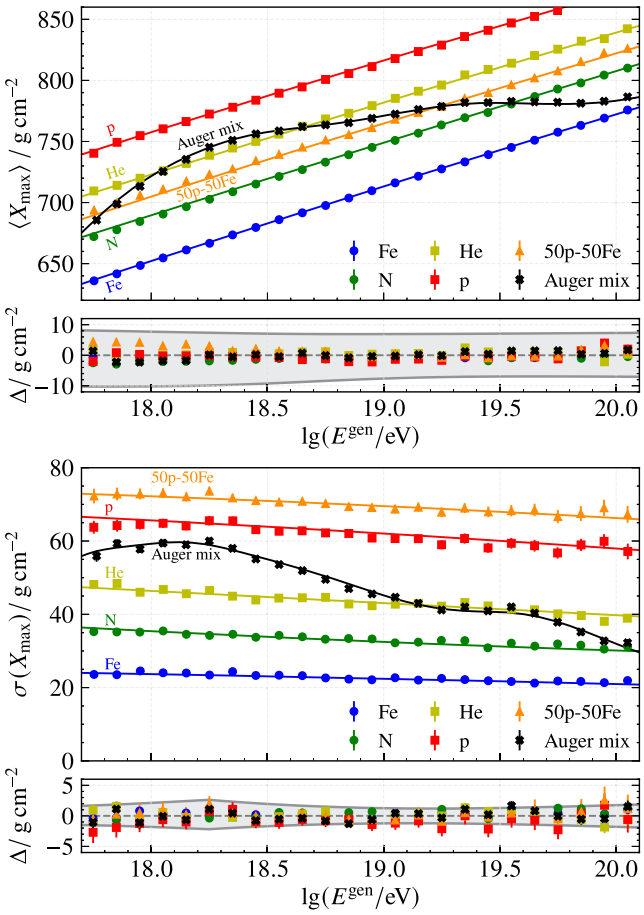


FIG. 10. $\langle X_{\rm max}\rangle$ and $\sigma(X_{\rm max})$ for simulated pure proton, helium, nitrogen, and iron primaries, a 50/50 proton-iron mixture, and the 4-component fractional composition derived in Sec. VII (Auger mix). The line indicates the true moments of the generated dataset, while points show the reconstructed values. The lower panel of each figure shows the difference Δ between reconstructed and generated values. Simulations use the hadronic model SIBYLL 2.3d.

from uncertainties in the acceptance, bias, and resolution corrections and are well within the systematic uncertainties discussed in Sec. IV C. We conclude that the analysis method performs well.

C. FD sites

The four FD sites are Los Leones (LL), Los Morados (LM), Loma Amarilla (LA), and Coihueco (CO). Each is constructed similarly, though there are site-to-site differences in placement, alignment, electronics, and other factors that can affect the reconstruction of $X_{\rm max}$. The top panel of Fig. 11 shows, for each site, the differences in $\langle X_{\rm max}\rangle$ and $\sigma(X_{\rm max})$ relative to the values obtained from the combined dataset. Testing the compatibility of these differences with zero for all sites simultaneously yields $\chi^2 = 97$ for $\langle X_{\rm max}\rangle$ and $\chi^2 = 40$ for $\sigma(X_{\rm max})$, both with 57 degrees of freedom. The incompatibility of $\Delta\langle X_{\rm max}\rangle$ with zero is largely driven by a systematic offset of a few g cm^{-2} for both CO and LM as compared to LL and LA in the energy range from $10^{17.7}$ eV to $10^{18.5}$ eV, likely related to site-dependent differences in the energy scale, as discussed in Ref. [57].

D. Geometry and atmospheric quality

The dataset has been split by zenith angle, atmospheric aerosol content, and distance to the event to probe different geometric and atmospheric effects. The differences between the $\langle X_{\rm max}\rangle$ values of the two subsets for each case are shown on the left of Fig. 11, while the differences in $\sigma(X_{\rm max})$ are shown on the right. The corresponding χ^2 values for compatibility with zero, indicating no observable dependence, are also shown. For all three data splits, the differences are well-contained within the systematic uncertainties for the atmosphere and detector presented in Sec. IV.

a. Inclined vs vertical showers Events are divided into *inclined* and *vertical* subsets at median$(\cos\theta) = 0.793 - 0.085\,\lg(E/\text{EeV})$. The altitude at which a given $X_{\rm max}$ occurs increases with zenith angle as inclined showers reach the same slant depth higher in the atmosphere. As a result, the detector acceptance and resolution differ between inclined and vertical events, potentially introducing a bias. This effect is evaluated in the second row of Fig. 11, which shows that the inclined subset is consistent with the vertical to better than 3 g cm^{-2} $\langle X_{\rm max}\rangle$. $\Delta\sigma(X_{\rm max})$ is compatible with zero.

b. Dusty vs clean atmospheres Events are divided into *clean* and *dusty* subsets at median(VAOD) $= 0.027 + 0.004\,\lg(E/\text{EeV})$. On nights with more atmospheric aerosols, the attenuation of fluorescence light on its way to the telescope is increased, and thus, potential biases in the aerosol determination are more important. This effect is investigated in the third row of Fig. 11, and shows that both $\Delta\langle X_{\rm max}\rangle$ and $\Delta\sigma(X_{\rm max})$ are compatible with zero.

c. Close versus distant showers Events are divided into *close* and *far* subsets at median $d = 10 + 9.6\,\lg(E/\text{EeV})$ km. This cross-check probes the understanding of the transmission through the atmosphere, which is more important for the more distant dataset. The result of this test is shown in the last row of Fig. 11, which shows that the differences in $\langle X_{\rm max}\rangle$ in the far subset are within 2.5 g cm^{-2} at low energies, and 3.5 g cm^{-2} at the highest energies. $\Delta\sigma(X_{\rm max})$ is compatible with zero.

E. Time evolution

Detector aging could introduce a time-dependent bias in the $X_{\rm max}$ reconstruction. Fig. 12 shows the yearly $\langle X_{\rm max}\rangle$ and $\sigma(X_{\rm max})$ values obtained from events at all energies, with linear fits applied to quantify the trends. The values of $\sigma(X_{\rm max})$ are found to be very stable in time within uncertainties, but a small time dependence of $\langle X_{\rm max}\rangle$ is

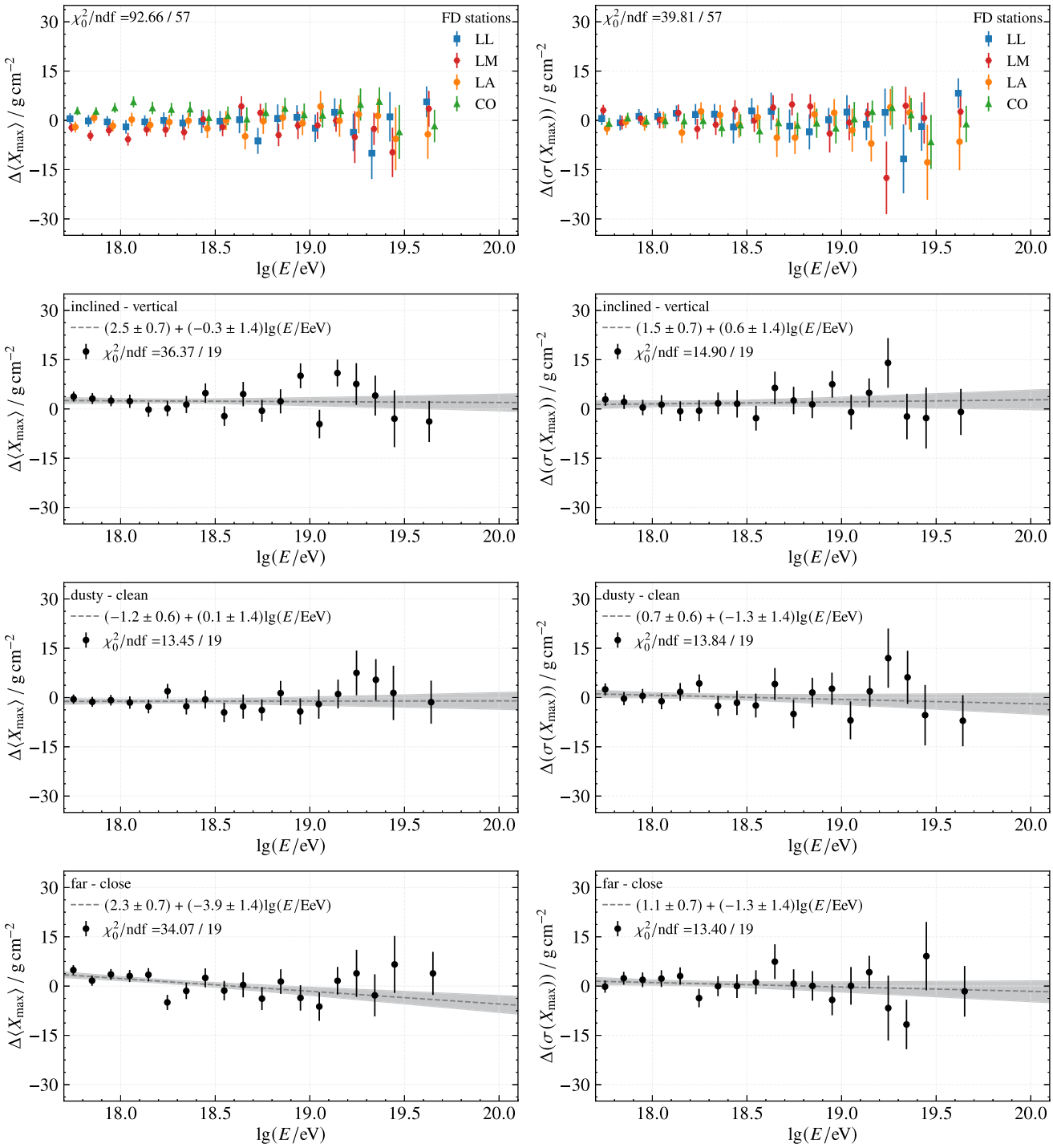


FIG. 11. Differences in the mean and standard deviation of the $X_{\rm max}$ distribution for various cross-checks. From top to bottom; events split by FD site (LL, LM, LA, CO), near-vertical versus inclined showers, dusty versus clean nights; and events close to the FD site versus those at larger distances. A linear fit to the data is shown as a dashed line with a gray uncertainty contour. The χ_0^2/ndf values for compatibility with zero are given, as are the linear fit values.

observed, of about +0.50 g cm^{-2}/year. Part of this effect can be attributed to changes in the optical response of the telescopes. Therefore, it should be regarded as part of the 14% energy-scale systematic uncertainty, as changes in energy translate into shifts of $\langle X_{\rm max}\rangle$ via the elongation rate, see Sec. VI. After applying the time-dependent response correction from [58], which is compatible with recent measurements of the optical efficiency [59], the remaining

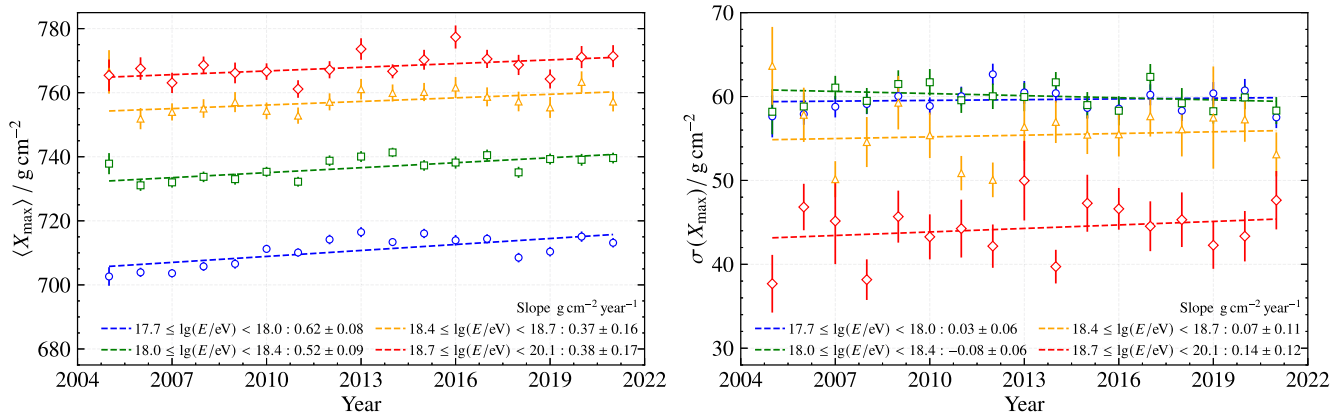


FIG. 12. Time evolution of the mean and standard deviation of $X_{\rm max}$ for four different energy bins. The dashed lines indicate linear fits, and the corresponding slopes are given in the legend.

change in $\langle X_{\rm max}\rangle$ amounts to about $+0.25$ g cm^{-2}/year. The origin of this residual effect is not known, but its magnitude is well within the overall systematic uncertainties. We therefore conclude that over the 17 years covered by this analysis, the $X_{\rm max}$ scale remains stable to within ± 2 g cm^{-2}.

F. Declination dependence of $X_{\rm max}$

The statistics of the FD dataset are sufficient to support an independent analysis of the $X_{\rm max}$ distributions obtained from the northern and southern portions of the exposure of the Observatory. The split between the northern and southern regions is made at a declination of $\delta = -15.7°$, which was chosen as it represents the southernmost extent of the FD hybrid composition sensitivity of the majority of Telescope Array analyses [60]. This data split results in 37 956 events in the southern subsample and 20 497 events in the northern subsample.

To prepare the $X_{\rm max}$ measurements from each subset of the sky, the corrections described in Sec. IV have been calculated separately for the northern and southern declination bands. The differences in reconstruction bias, resolution, and other systematics were found to be negligible. Minor differences in $X_{\rm max}$-dependent event acceptance were observed. The systematic uncertainties in the comparison between the two regions arising from these corrections were found to be less than 2 g cm^{-2} in any bin.

After these corrections, the first two moments of the $X_{\rm max}$ distributions in the two declination bands were calculated and compared in Fig. 13. Overall, good agreement is observed between the two regions. In the highest-energy bin, however, where statistics are limited, a larger difference does appear, with the northern portion of the sky having, on average, shallower $X_{\rm max}$ values. To evaluate any possible significance, a detailed statistical comparison of the two samples was performed using the Kolmogorov-Smirnov [61] and Anderson-Darling [62] two-sample tests in each energy bin. No statistically significant difference was found in any bin.

These results indicate that, within the exposure of the Observatory, there is no evidence for a declination dependence in the mass composition of UHECRs. This conclusion is consistent with the findings of the joint composition working group with the Telescope Array [63] and aligns

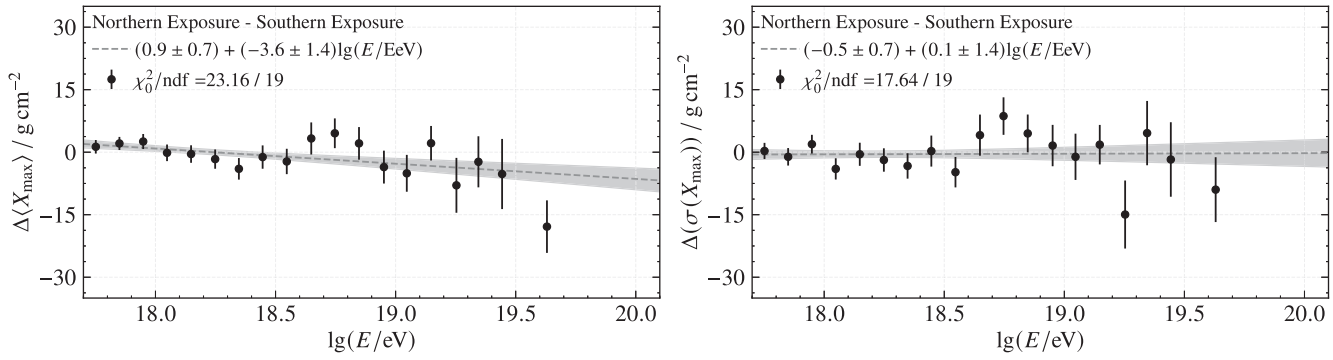


FIG. 13. Comparison of events arriving from northern ($\delta \geq -15.7°$) and southern ($\delta < -15.7°$) portions of the FD exposure. Left: The difference (north—south) in $\langle X_{\rm max}\rangle$. Right: The difference (north—south) in $\sigma(X_{\rm max})$. A linear fit to the data is shown as a dashed line with a gray uncertainty contour. The χ^2_0/ndf values for compatibility with zero are given, as are the linear fit values.

with the absence of declination-dependent features in the UHECR energy spectrum reported by us in Ref. [64].

G. Assessment of validation studies

The extensive validation studies demonstrate excellent stability and reliability of the $X_{\max}$ reconstruction and analysis. The detector resolution derived from simulation agrees with the resolution measured in stereo events, and the full end-to-end analysis of simulated events reproduces generated $\langle X_{\max}\rangle$ and $\sigma(X_{\max})$ values within the assigned systematic uncertainties. Site-to-site differences, geometric and atmospheric dependencies, and temporal effects are small and consistent with expectations and known uncertainties. The comparison of northern and southern declination bands shows no statistically significant differences. Overall, the cross-checks indicate that no unaccounted systematic effects are present.

VI. MOMENTS OF $X_{\max}$ AND $\ln A$

After applying the event selection and correcting for biases in $X_{\max}$, the observed $X_{\max}$ distributions exhibit minimal biases with respect to the true distributions.

To enable comparison to the unbiased moments obtained directly from the simulated showers at generator level, the residual bias of the acceptance on the mean and standard deviation is corrected for using the Λ_η method as detailed in Ref. [16]. In this method, the observed $X_{\max}$ distribution is used directly in the region of constant acceptance, while its tails are described by exponential functions fitted with the acceptance taken into account; here, η denotes the fraction of events in a given tail used for the fit, with $\eta = 0.20$ for the deep tail and $\eta = 0.15$ for the leading edge. The moments are then obtained from this combined distribution. This correction to the moments from the residual acceptance bias is found to be small, reaching at most 3 $\mathrm{g\,cm^{-2}}$ for $\langle X_{\max}\rangle$ and 5 $\mathrm{g\,cm^{-2}}$ for $\sigma(X_{\max})$, depending on energy. The $X_{\max}$ resolution is then subtracted from $\sigma(X_{\max})$ in quadrature. Statistical uncertainties are calculated using a parametric bootstrap method described in [16]. The numerical values of $\langle X_{\max}\rangle$ and $\sigma(X_{\max})$ are listed in Table V (Appendix E).

The energy evolution of $\langle X_{\max}\rangle$ is shown in Fig. 14. The *elongation rate*,

$$D_{10} = \frac{\mathrm{d}\langle X_{\max}\rangle}{\mathrm{d}\lg E}, \tag{5}$$

exhibits a distinct transition from

$$D_{10} = 81.8 \pm 1.7(\mathrm{stat})\,^{+1.9}_{-3.0}(\mathrm{sys})\ \mathrm{g\,cm^{-2}/decade} \tag{6}$$

below $\lg(E_{\mathrm{break}}/\mathrm{eV}) = 18.38 \pm 0.02(\mathrm{stat})^{+0.01}_{-0.01}(\mathrm{sys})$ to

$$D_{10} = 25.7 \pm 1.9(\mathrm{stat})\,^{+5.3}_{-1.5}(\mathrm{sys})\ \mathrm{g\,cm^{-2}/decade} \tag{7}$$

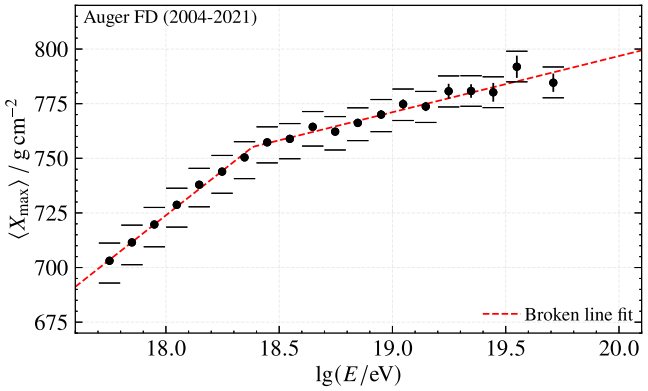


FIG. 14. Energy evolution of $\langle X_{\max}\rangle$. Statistical uncertainties are displayed using vertical error bars, while systematic uncertainties are indicated by horizontal caps above and below the markers. The red line shows a broken-line fit to the data.

above the break, in good agreement with the value of $24.1 \pm 1.2(\mathrm{stat})$ $\mathrm{g\,cm^{-2}/decade}$ derived from SD data above $10^{18.5}$ eV [65]. Note that the uncertainty quoted on $\lg(E_{\mathrm{break}})$ does not include the energy scale uncertainty of 14%. The best-fit average shower maximum at $\lg(E_{\mathrm{break}})$ is $X^{\mathrm{break}}_{\max} = 755.2 \pm 1.5(\mathrm{stat})\,^{+5.3}_{-10.6}(\mathrm{sys})$ $\mathrm{g\,cm^{-2}}$. The corresponding fit is shown as a red dashed line in Fig. 14 and results in a goodness of fit of $\chi^2/\mathrm{ndf} = 18.4/16$ (p-value $= 0.30$), indicating a good agreement with the data. In contrast, a model using a single line is decisively rejected by the data ($\chi^2/\mathrm{ndf} = 512/18$). Including two additional breaks at higher energies, as observed with the surface detector [65], does not significantly improve the fit quality.

The observed elongation rates provide robust, model-independent evidence with high statistical significance that the composition is changing in the observed energy range, since for a constant composition the elongation rate would remain constant [3,66].

Since $\langle X_{\max}\rangle$ depends linearly on $\langle \ln A\rangle$, Eq. (5) implies that D_{10} is linear in $\mathrm{d}\langle \ln A\rangle/\mathrm{d}\lg E$. Air shower simulations using the latest models of hadronic interactions at ultrahigh energies predict an elongation rate in the range of 55 to 60 $\mathrm{g\,cm^{-2}/decade}$ for a constant composition. Therefore, the large elongation rate measured below the break, Eq. (6), implies a transition from heavier to light composition. Likewise, the smaller D_{10}, above the break, Eq. (7), indicates a transition from light to a heavier composition.

Along with this change of the mean $X_{\max}$, we also observe a decrease in the standard deviation of the $X_{\max}$ distribution, $\sigma(X_{\max})$. It is shown in the right panel of Fig. 15. Whereas a large value of $\sigma(X_{\max})$ can indicate either a light or mixed composition, the pronounced decrease of $\sigma(X_{\max})$ from 60 to 30 $\mathrm{g\,cm^{-2}}$ is another model-independent indicator for a transition to predominantly heavy cosmic-ray nuclei at ultrahigh energies.

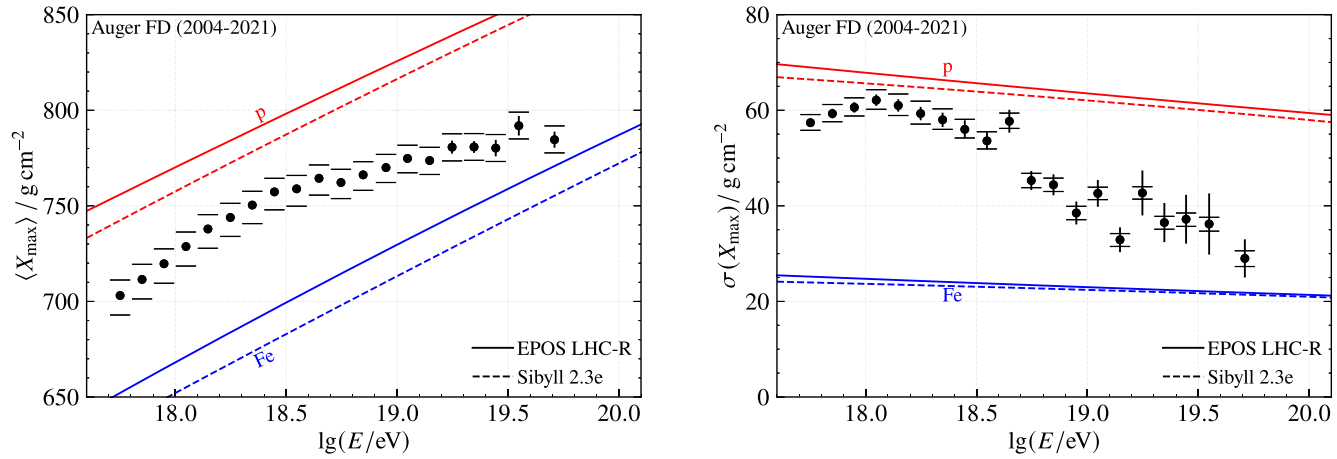


FIG. 15. Energy evolution of $\langle X_{\rm max}\rangle$ and $\sigma(X_{\rm max})$ compared to the predictions from air-shower simulations using the hadronic interaction models EPOS LHC-R and SIBYLL 2.3e for proton and iron primaries. Statistical uncertainties are displayed by vertical error bars, while systematic uncertainties are indicated by horizontal caps above and below the markers.

In the energy bin $18.6 \leq \lg(E/\text{eV}) < 18.7$, the $\sigma(X_{\rm max})$ value is considerably larger than expected from an interpolation between the neighboring energy bins. The local significance of the deviation of $\sigma(X_{\rm max})$ in this bin from the overall trend, evaluated by excluding the bin from a fit with a smooth curve to the data, is 3.4σ. The global significance of observing such a fluctuation in any energy bin is 2.4σ.

It is worth noting that an event with an exceptionally deep $X_{\rm max}$ of about 1200 g cm^{-2} was recorded in this interval. Excluding this event reduces $\sigma(X_{\rm max})$ by only 1 g cm^{-2}, indicating that it does not drive the observed increase. The event is consistent with an extreme fluctuation of a proton-initiated shower; further details are given in Sec. A.

For further, but more model-dependent, insights into the cosmic-ray composition, we compare in Fig. 15 the measured $\langle X_{\rm max}\rangle$ and $\sigma(X_{\rm max})$ to the predictions of SIBYLL 2.3e [10] and EPOS LHC-R [12] for protons and iron.[1] This allows an interpretation of how the absolute values of $\langle X_{\rm max}\rangle$ and $\sigma(X_{\rm max})$ evolve between proton- and iron-induced showers. The observed $\langle X_{\rm max}\rangle$ is close to predictions for helium at $E_{\rm break}$. At the highest energies, both $\langle X_{\rm max}\rangle$ and $\sigma(X_{\rm max})$ evolve toward the predictions for iron, although within the current statistics also a somewhat lighter, intermediate average mass of cosmic rays is compatible with the data.

The measured $\langle X_{\rm max}\rangle$ and $\sigma(X_{\rm max})$ in each energy bin can be converted into the first two central moments of the logarithmic mass, using the method described in Refs. [7,67], and the parametrizations from [68], see Fig. 16. Due to the small variations in the model predictions of the $\langle X_{\rm max}\rangle$ elongation rate, a similar energy dependence is observed in $\langle \ln A\rangle$ for both interaction models. Below $E_{\rm break}$ we obtain

$$\frac{\mathrm{d}\langle \ln A\rangle}{\mathrm{d}\lg E} = -0.94 \pm 0.07(\text{stat})\,^{+0.14}_{-0.07}(\text{sys}) \pm 0.05(\text{model}),$$

and above $E_{\rm break}$

$$\frac{\mathrm{d}\langle \ln A\rangle}{\mathrm{d}\lg E} = +1.26 \pm 0.08(\text{stat})\,^{+0.10}_{-0.21}(\text{sys}) \pm 0.01(\text{model}).$$

The spread among the model predictions of $\langle X_{\rm max}\rangle$ translates into a difference of about 0.5 in $\langle \ln A\rangle$, with EPOS LHC-R yielding a heavier and SIBYLL 2.3e a lighter average mass composition. At the highest energies, the estimated mean logarithmic masses from both models are close to the CNO group. The variances of $\ln A$ are similar and indicate an increase in mass mixing below $10^{18.1}$ eV, where they reach their maximum values. Above this energy, $\mathrm{Var}(\ln A)$ decreases until approximately $10^{18.8}$ eV.

At higher energies, $\mathrm{Var}(\ln A)$ shows no clear trend and remains approximately constant at 0.3–0.5, consistent with expectations for equal mixtures of adjacent mass groups (p-He, He-CNO, CNO-Fe). However, pure or more broadly mixed compositions cannot be ruled out within the current uncertainties.

VII. MASS FRACTIONS

The mean and variance of $\ln A$ cannot be interpreted unambiguously in terms of the relative fractions of primary nuclei, i.e. the mass fractions. Instead, the observed $X_{\rm max}$ distributions can be fitted with a superposition of simulated

[1]We defer comparisons with the newest version of the QGSJet model (QGSJET iii-01 [11]) to future work, pending resolution of a technical issue in the current implementation that affects simulated nucleus-nucleus interactions (S. Ostapchenko, private communication).

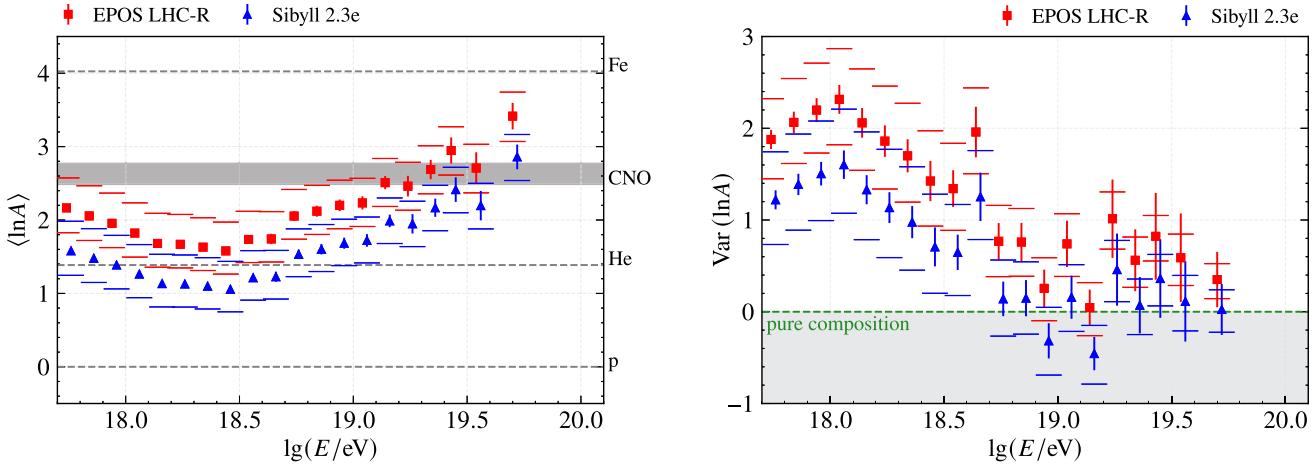


FIG. 16. Energy evolution of $\langle \ln A \rangle$ and $\mathrm{Var}(\ln A)$ estimated using air-shower simulations with the hadronic interaction models EPOS LHC-R and SIBYLL 2.3e. Statistical uncertainties are represented by vertical error bars, and systematic uncertainties are indicated by horizontal caps above and below the markers.

$X_{\max}$ distributions for different nuclei using their relative fractions as fit parameters. In our previous work [17], we demonstrated that satisfactory fits to the data can be achieved using at least four species representing light, intermediate, and heavy mass groups. Specifically, we used protons and three representative nuclei (helium, nitrogen, and iron), nearly equally spaced in $\ln A$, and investigated the energy evolution of the mass fractions of these four species.

A. Templates for Monte Carlo simulations of $X_{\max}$

The $X_{\max}$ distributions used for comparison with the data are generated using the CONEX air-shower program [48] for two hadronic interaction models: EPOS LHC-R and SIBYLL 2.3e. To account for the effects of detector acceptance and resolution, these distributions are modified according to Eqs. (4) and (3). The resulting composition *templates* are binned in $X_{\max}$ over a range from 0 to 2000 $\mathrm{g\,cm^{-2}}$, with a bin width of 10 $\mathrm{g\,cm^{-2}}$. The energy distribution in each energy bin follows a power law $E^{-\alpha}$, where the spectral index α is estimated using the energy distribution of the selected events (cf. Fig. 3). We use $\alpha = 1.1$ for energies below $10^{18.0}$ eV and $\alpha = 2.2$ for higher energies. Above $10^{19.6}$ eV, the spectral index is estimated as $\alpha = 4.7$.

Because both the hybrid exposure [46] and the fiducial selection efficiency increase with energy, these values of α for the observed energy distribution differ significantly from the spectral indices of the UHECR energy spectrum.

B. Fitting procedure

A Poissonian binned maximum-likelihood approach is used [56] to determine the best-fitting combination of primary species, with the likelihood function described in Ref. [17]. To estimate the posterior distribution of the mass fractions, we apply a Bayesian Markov chain Monte Carlo method, using the sampler described in Ref. [69]. The mass fractions are restricted to the interval [0, 1] and are constrained to sum to unity. A symmetric Dirichlet (1, 1, 1, 1) prior is adopted for the fractions, corresponding to a uniform prior over all allowed combinations of non-negative fractions. We use the maximum a-posteriori estimator to provide numerical values that characterize the posterior distribution from the fit. The statistical uncertainties on the estimated composition fractions are expressed using the 68% highest-posterior-density interval, representing the 1σ confidence range. An example of a fit and the one- and two-dimensional posterior probabilities are shown in Figs. 17 and 18. The fitted

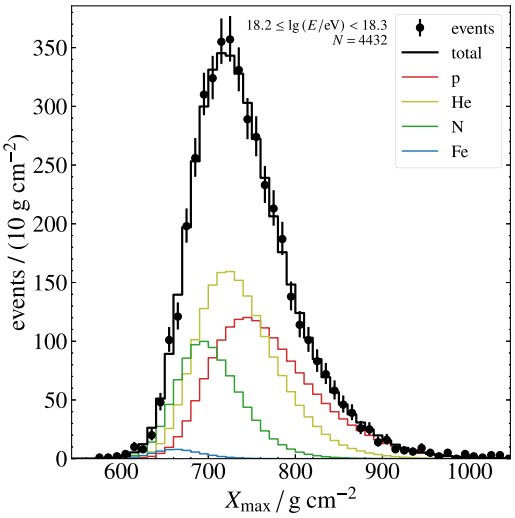


FIG. 17. Example of the fit of composition fractions of the mass groups (H, He, N, Fe) with SIBYLL 2.3e in the energy range $18.2 \le \lg(E/\mathrm{eV}) < 18.3$; $X_{\max}$ distribution of the data (points with error bars) and composition templates (histograms) scaled by their fitted fractions.

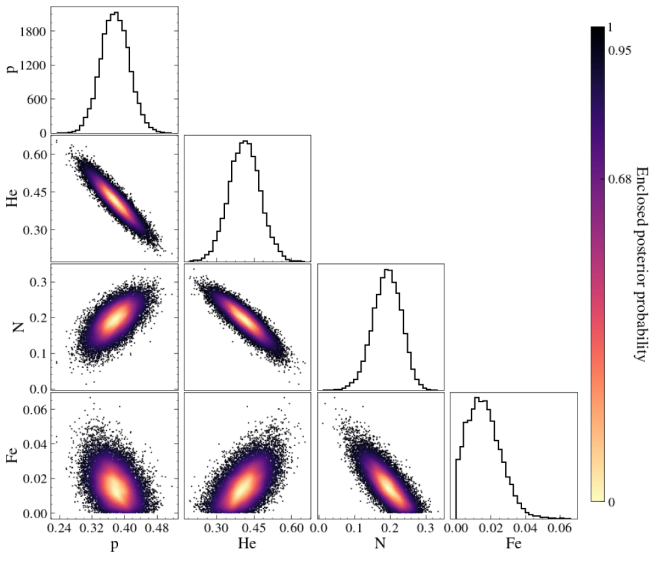


FIG. 18. Corner plot of the posterior mass-fraction parameters for H, He, N, and Fe obtained with SIBYLL 2.3e in the energy range $18.2 \leq \lg(E/\mathrm{eV}) < 18.3$. The diagonal panels show the one-dimensional marginalized posteriors for each group, while the off-diagonal panels show the two-dimensional joint posteriors (pairwise correlations). Colors indicate the enclosed posterior probability, with the lighter colors corresponding to regions of higher posterior density.

X_{max} distributions for all energies and both interaction models are presented in Appendix D. As can be seen, because of the large overlap of the X_{max} distribution of different mass groups, the fractions of neighboring groups are negatively correlated.

To evaluate the fit quality, the X_{max} distributions for the best-fit mass fractions are used to generate mock samples of the same size as the data. The likelihood of each mock sample with respect to the best-fit model is compared to the likelihood found for the data to count the fraction of worse fits. This fraction, the p-value, is a statistical measure of how well the best-fit model represents the underlying data.

C. Systematic uncertainties

Alongside the statistical uncertainties, we evaluate the systematic uncertainties on the fitted mass fractions, primarily arising from the systematic uncertainty in X_{max}. This contribution is evaluated by varying the X_{max} scale within its uncertainty range using steps of $0.1(\sigma_{\mathrm{low}} + \sigma_{\mathrm{up}})$, where σ_{low} and σ_{up} represent the lower and upper bounds of the systematic-uncertainty intervals. This approach is necessary due to the nonmonotonic relationship between the fractions and changes in the X_{max} scale. We refit the shifted and rebinned data, taking the largest and smallest obtained fractions as the limits of the lower and upper systematic uncertainties. Similarly, the smallest and largest p-values identified in this procedure serve as systematic uncertainties on the p-values. Another source of systematic uncertainty arises from the energy scale, which is evaluated by refitting the data after shifting the energy scale by $\pm 14\%$. As a cross-check, the mass fractions were also evaluated within the frequentist approach previously used in Ref. [17]. The results were found to be consistent with the Bayesian method. Finally, we estimated the contribution from uncertainties in the parametrization of the detector acceptance and resolution by re-fitting the data using extreme values of the parametrizations.

D. Results

The results for the determined mass fractions of protons, helium, nitrogen and iron nuclei are shown in Fig. 19, using EPOS LHC-R and SIBYLL 2.3e. The p-values are shown in the lower panel and indicate an overall good agreement between the data and the model predictions. Over most of the energy range, the p-values are compatible with $p \gtrsim 10^{-1}$, except in three energy bins where they drop by several orders of magnitude. We verified that, in these bins, the p-values improve by at most one order of magnitude when excluding the "outliers" discussed in Sec. A or when adding an intermediate heavy mass group, represented by silicon, to the fit.

The cosmic-ray mass composition obtained with SIBYLL 2.3e contains an approximately equal proton-helium-nitrogen mixture at the lowest energies, with helium becoming dominant above $10^{18.5}$ eV followed by a transition to nitrogen dominance above $10^{19.0}$ eV. The iron contribution remains consistent with zero within uncertainties at all energies. These results align qualitatively and quantitatively with our previous estimates [17]. In contrast, the composition inferred using EPOS LHC-R is heavier owing to its deeper X_{max} scale (cf. Figs. 15 and 16). The nitrogen fraction increases from approximately 50% at the lowest energies to above 80% above the ankle, before the iron contribution becomes significant at the highest energies, accounting for about half of the total mix. The helium fraction derived from EPOS LHC-R remains at a level of 5–10% across the entire energy range and shows no systematic trend with energy.

The qualitative behavior of the proton fraction is consistent for both models. This can be understood in terms of the evolution of the X_{max} fluctuations, which, like the proton fraction, first increase and then decrease as the deep tails of the X_{max} distributions die out (Figs. 15 and 4).

VIII. SUMMARY AND CONCLUSION

In this paper, we have presented measurements of the X_{max} distributions with minimal selection bias using the hybrid data of the Pierre Auger Observatory. The dataset comprises 58,453 high-quality events with energies above $10^{17.7}$ eV. The most energetic event has an energy of about 1.17×10^{20} eV.

The mean and standard deviation of the X_{max} distributions have been corrected for the residual biases, enabling direct comparison to current and future predictions from

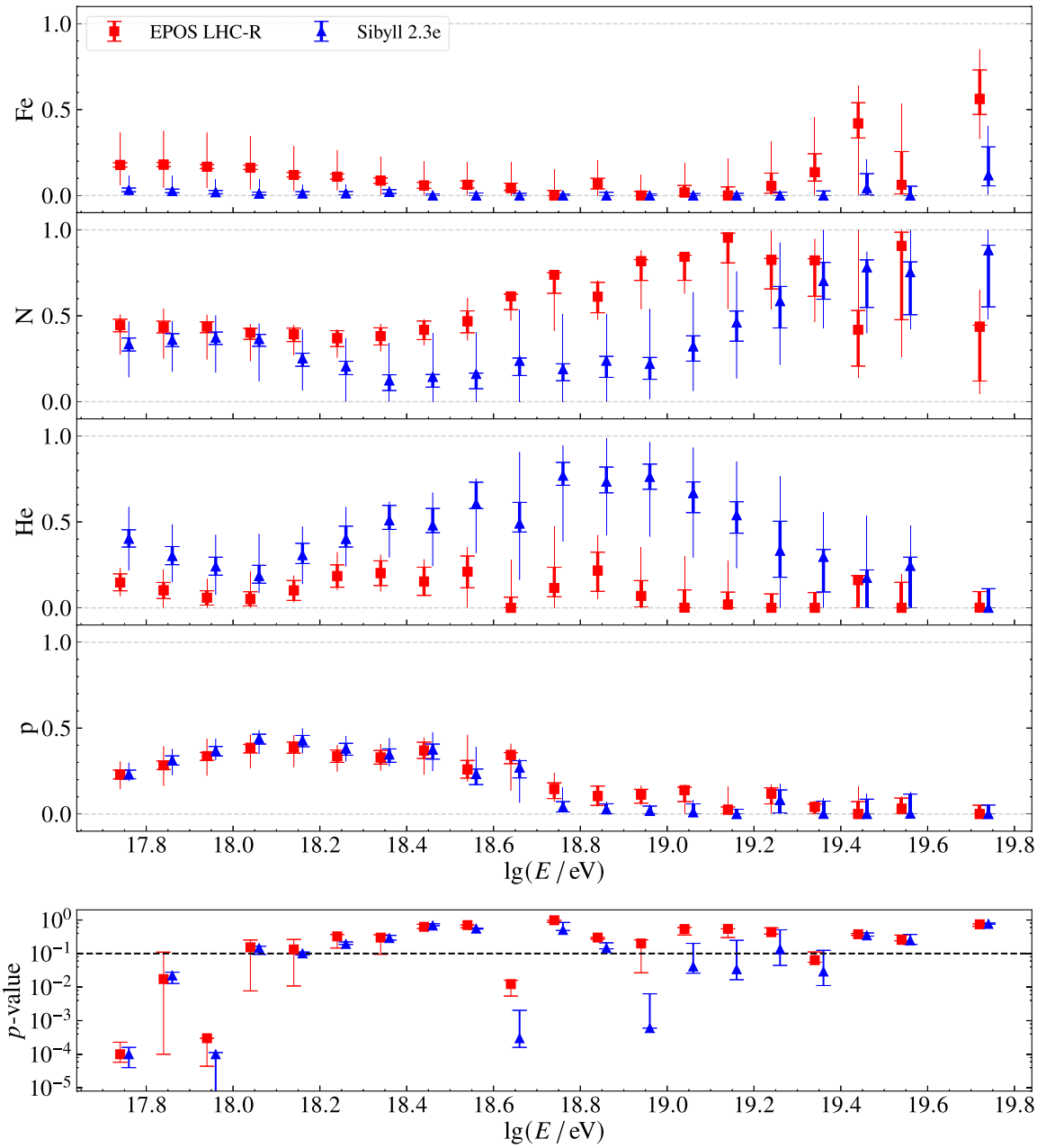


FIG. 19. Top four panels: best-fit fractions of protons, helium, nitrogen, and iron nuclei using air-shower simulations with the SIBYLL 2.3e and EPOS LHC-R hadronic interactions models. The error bars denote statistical (thick lines) and total (thin lines) uncertainties. Bottom panel: p-values of the fit. The error bars denote systematic uncertainties.

air-shower simulations. From these measurements, we draw two key observations that are independent of theoretical uncertainties of the modeling of hadronic interactions at ultrahigh energies.[2] First, the rate at which $\langle X_{\rm max}\rangle$ evolves with the logarithm of energy exhibits a marked change at $\approx 10^{18.4}$ eV, providing evidence that the trend toward lighter mass composition reverses at this energy. Second, the $X_{\rm max}$ distributions become narrower above approximately the same energy, indicating a transition to a heavier and less-mixed mass composition. A comparison of the $X_{\rm max}$ distributions in the northern and southern declination bands of the Observatory's exposure shows no statistically significant difference, indicating no directional dependence of the mass composition.

For a more direct interpretation of these findings, we have converted $X_{\rm max}$ moments into $\langle \ln A\rangle$ and $\mathrm{Var}(\ln A)$ using the interaction models EPOS LHC-R and SIBYLL 2.3e.

[2]These conclusions assume that no qualitatively new high-energy physics processes alter air-shower development at ultrahigh energies. For speculative scenarios in which this assumption could be violated, see, e.g., Refs. [70,71].

The universality of model predictions for the $\langle X_{\max}\rangle$ elongation rate leads to similar $\langle \ln A\rangle$ energy evolution for both models, with $\mathrm{d}\langle \ln A\rangle/\mathrm{d}\lg E$ changing from -0.94 to $+1.26$ at the $\langle X_{\max}\rangle$ break. At the highest energies, the $\langle \ln A\rangle$ values inferred with both models suggest an average mass approaching that of the CNO group. The spread of the primary masses increases until $10^{18.1}$ eV after which it decreases until approximately $10^{18.8}$ eV. Beyond this energy, $\mathrm{Var}(\ln A)$ fluctuates around 0.5 without exhibiting a clear trend, and it remains compatible with a pure or more mixed composition within the uncertainties.

Finally, we have used the measured $X_{\max}$ distributions to examine the energy evolution of four primary mass groups, protons, helium, nitrogen, and iron nuclei. We observe similar general trends with the proton contribution peaking around $10^{18.1}$ eV and nearly disappearing above the ankle in the cosmic-ray energy spectrum. As the proton fraction decreases, the relative contribution of intermediate-mass nuclei increases, with helium dominating near the ankle in SIBYLL 2.3e and nitrogen in EPOS LHC-R. The difference is due to the deeper $X_{\max}$ scale of EPOS LHC-R that is also favored by our analyses combining $X_{\max}$ and the SD signal [58,72–74]. At higher energies, nitrogen becomes dominant, with the iron fraction remaining negligible in SIBYLL 2.3e but gradually increasing toward the highest energies in EPOS LHC-R.

The events selected for this analysis represent an unprecedented dataset of direct observations of the energy and depth of maximum of air-shower profiles. As demonstrated in the paper, our measurements provide unique insights into the mass composition of UHECRs across two decades in energy. Importantly, this dataset serves as the reference for calibration of indirect $X_{\max}$ inferences from the surface detector data [65,75–77]. The list of $X_{\max}$ and energy of each event used in this analysis, as well as the derived measurements of $X_{\max}$ and $\ln A$ moments and the posterior samples of mass fractions are available for download from Ref. [45]. Together with the information provided in Appendix B on the acceptance and resolution, this unique data set can be used for self-contained studies of mass composition and hadronic interactions.

ACKNOWLEDGMENTS

The successful installation, commissioning, and operation of the Pierre Auger Observatory would not have been possible without the strong commitment and effort from the technical and administrative staff in Malargüe. We are very grateful to the following agencies and organizations for financial support: Argentina—Comisión Nacional de Energía Atómica; Agencia Nacional de Promoción Científica y Tecnológica (ANPCyT); Consejo Nacional de Investigaciones Científicas y Técnicas (CONICET); Gobierno de la Provincia de Mendoza; Municipalidad de Malargüe; NDM Holdings and Valle Las Leñas; in gratitude for their continuing cooperation over land access; Australia—the Australian Research Council; Belgium—Fonds de la Recherche Scientifique (FNRS); Research Foundation Flanders (FWO), Marie Curie Action of the European Union Grant No. 101107047; Brazil—Ministério da Ciência, Tecnologia e Inovação (MCTI); Czech Republic—GACR 24-13049S, CAS LQ100102401, MEYS LM2023032, CZ.02.1.01/0.0/0.0/16_013/0001402, CZ.02.1.01/0.0/0.0/18_046/0016010 and CZ.02.1.01/0.0/0.0/17_049/0008422 and CZ.02.01.01/00/22_008/0004632; France—Centre de Calcul IN2P3/CNRS; Centre National de la Recherche Scientifique (CNRS); Institut National de Physique Nucléaire et de Physique des Particules (IN2P3/CNRS); Germany—Bundesministerium für Forschung, Technologie und Raumfahrt (BMFTR); Deutsche Forschungsgemeinschaft (DFG); Ministerium für Finanzen Baden-Württemberg; Helmholtz Alliance for Astroparticle Physics (HAP); Hermann von Helmholtz-Gemeinschaft Deutscher Forschungszentren e.V.; Ministerium für Kultur und Wissenschaft des Landes Nordrhein-Westfalen; Ministerium für Wissenschaft, Forschung und Kunst des Landes Baden-Württemberg; Italy—Istituto Nazionale di Fisica Nucleare (INFN); Istituto Nazionale di Astrofisica (INAF); Ministero dell'Università e della Ricerca (MUR); CETEMPS Center of Excellence; Ministero degli Affari Esteri (MAE), ICSC Centro Nazionale di Ricerca in High Performance Computing, Big Data and Quantum Computing, funded by European Union NextGenerationEU, reference code CN_00000013; México—Consejo Nacional de Ciencia y Tecnología (CONACYT-SECHTI) No. CB-A1-S-46703, Universidad Nacional Autónoma de México (UNAM) PAPIIT-IN114924; Benemérita Universidad Autónoma de Puebla (BUAP), VIEP and Laboratorio Nacional de Supercómputo del Sureste de México (LNS); and Benemérita Universidad Autónoma de Chiapas (UNACH); The Netherlands—Ministry of Education, Culture and Science; Netherlands Organisation for Scientific Research (NWO); Dutch national e-infrastructure with the support of SURF Cooperative; Poland—Ministry of Science and Higher Education, grant No. 2022/WK/12; National Science Centre, Grants No. 2020/39/B/ST9/01398, and No. 2022/45/B/ST9/02163; Portugal—Portuguese national funds and FEDER funds within Programa Operacional Factores de Competitividade through Fundação para a Ciência e a Tecnologia (COMPETE); Romania—Ministry of Education and Research, Contract No. 30N/2023 under Romanian National Core Program LAPLAS VII, and Grant No. PN 23 21 01 02; Slovenia—Slovenian Research and Innovation Agency, grants P1-0031, I0-0033; Spain—Ministerio de Ciencia, Innovación y Universidades/Agencia Estatal de Investigación MICIU/AEI /10.13039/501100011033 (PID2022-140510NB-I00, PCI2023-145952-2, CNS2024-154676, and María de Maeztu CEX2023-001318-M), Xunta de Galicia (CIGUS

Network of Research Centers, Consolidación ED431C-2025/11 and ED431F-2022/15) and European Union ERDF; USA—Department of Energy, Contracts No. DE-AC02-07CH11359, No. DE-FR02-04ER41300, No. DE-FG02-99ER41107, and No. DE-SC0011689; National Science Foundation, Grants No. 0450696, and No. NSF-2013199; The Grainger Foundation; Astrophysics Centre for Multimessenger studies in Europe (ACME) EU Grant No. 101131928; and UNESCO.

DATA AVAILABILITY

Data and tables available at [78] (referenced in the article).

APPENDIX A: EXTREME SHOWER EVENTS

1. Deepest event in the data sample

Event No. 53725865 is the deepest event observed in this dataset. Its image in one of the cameras of the Los Morados site and the corresponding longitudinal profile are shown in Fig. 20. The fit of the longitudinal profile yields $X_{\mathrm{max,LM}} = 1206 \pm 38\ \mathrm{g\,cm^{-2}}$ and an energy of $E_{\mathrm{LM}} = 4.2 \pm 0.6$ EeV. An independent reconstruction using data from a second FD site (Loma Amarilla) yields compatible values of $X_{\mathrm{max,LA}} = 1168 \pm 90\ \mathrm{g\,cm^{-2}}$ and $E_{\mathrm{LA}} = 3.9 \pm 0.5$ EeV, but this reconstruction does not pass the quality cuts. In the following, we test whether the event, given its X_{max}, is compatible with a deeply penetrating shower induced by a proton.

The corresponding probabilities, derived from air-shower simulations, are listed in Table II. In all cases discussed below, detector acceptance and X_{max} resolution are taken into account, and the quoted uncertainties are statistical.

As a first step, we assume the event is a proton primary with energy $E = E_{\mathrm{LM}}$ and compute the probability $p(E)$ that any single proton shower is reconstructed with an X_{max} value at least as large as the one observed. This probability is below 0.006%.

To account for the fact that multiple proton events are observed in the same energy bin, we compute the penalized probability $\tilde{p}(E)$ by multiplying $p(E)$ with the expected number of protons in that bin, using the proton fraction from Sec. VII for the relevant interaction model. This yields a probability of order 1%.

Finally, we extend the calculation to the full dataset to obtain p_{full}. For this, we simulate the full energy range using the measured composition from Sec. VII and count how often a shower is observed whose X_{max} exceeds the proton mean by at least as much as event No. 53725865 exceeds the proton mean at its energy. The resulting fully penalized probabilities range from about 0.2 to 0.6, depending on the interaction model.

We therefore conclude that, while event No. 53725865 is a remarkably deep shower, it is entirely compatible with expectations, given the fitted proton fractions from Sec. VII.

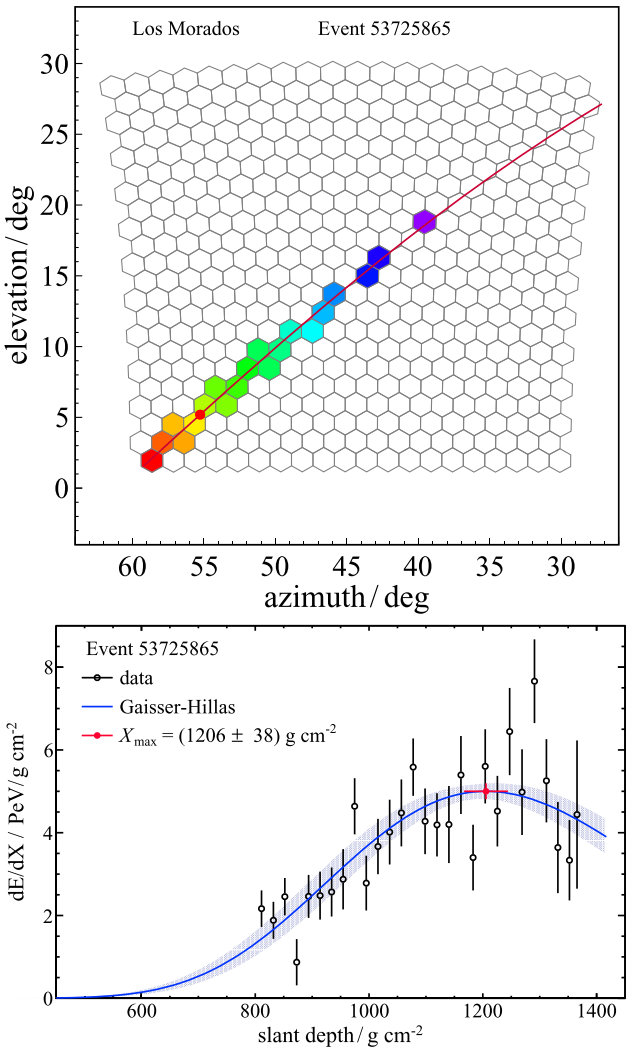


FIG. 20. Reconstruction of the deep shower event #53725865. Top panel: Camera view of the event. Colors denote the arrival time of photons in the hexagonal photomultipliers, with blue to red corresponding to early to late arrival times. The red line indicates the fitted shower–detector plane. Bottom panel: Longitudinal energy-deposit profile and fit with a Gaisser-Hillas function.

2. "Shallow" showers

Next, we characterize the number of shallow showers in the dataset using the condition

$$X_{\mathrm{max}} < X_0 + D_{10} \lg(E/\mathrm{EeV}), \tag{A1}$$

where $X_0 = 550\ \mathrm{g\,cm^{-2}}$ corresponds to a value 100 $\mathrm{g\,cm^{-2}}$ below the expected X_{max} for iron primaries at 1 EeV, and $D_{10} = 60\ \mathrm{g\,cm^{-2}}$ is the elongation rate expected for a constant mass composition. With this definition, we find

TABLE II. Probabilities to observe a proton shower at least as deep as event #53725865. The first column gives the probability for protons at the energy of the observed event, E. The second column includes the trial factor, taking into account the number of proton events expected in the energy bin containing the event. The third column extends the trial factor to all protons in the full dataset.

Model	$p(E)/10^{-5}$	$\tilde{p}(E)$	p_{full}
EPOS LHC-R	5.6 ± 0.8	0.025 ± 0.003	0.58 ± 0.01
SIBYLL 2.3e	2.0 ± 0.3	0.007 ± 0.001	0.24 ± 0.01

seven shallow showers in the dataset. For simulated events generated using the SIBYLL 2.3e hadronic interaction model, assuming an energy spectrum and mass composition consistent with the data, we expect 5 ± 2 shallow events. We therefore conclude that the dataset does not contain events with an unexpectedly shallow depth of shower maximum.

APPENDIX B: PARAMETRIZATIONS

1. Acceptance

The energy dependence of the acceptance parameters $\mathbf{p} = (X_1, X_2, \lambda_1, \lambda_2)$, introduced in Eq. (3), can be described by second-order polynomials in $x_{18} = \lg(E/10^{18}\ \text{eV})$,

$$p_i = \sum_{j=0}^{2} a_{ij}\, x_{18}^{j}. \tag{B1}$$

TABLE III. Parameters for X_1, X_2, λ_1 and λ_2.

	a_0	a_1	a_2
X_1	599.0 ± 1.0	46.1 ± 2.6	-19.0 ± 1.7
X_2	882.5 ± 0.9	49.9 ± 1.9	-21.8 ± 1.0
λ_1	122.8 ± 0.9	195.0 ± 3.4	35.5 ± 3.4
λ_2	108.9 ± 0.7	74.0 ± 1.6	9.1 ± 1.0

TABLE IV. Parameters of the X_{max} resolution, Eq. (4). σ_1 and σ_2 are given in g cm^{-2}. The uncertainties are systematic and originate from the uncertainty on the overall standard deviation of the resolution. They therefore shift σ_1 and σ_2 in the same direction and are fully positively correlated.

$\lg(E/\text{eV})$	σ_1	σ_2	f
17.7-17.8	18.9 ± 0.9	32.5 ± 1.6	0.71
17.8–17.9	17.7 ± 0.9	31.2 ± 1.5	0.72
17.9–18.0	16.7 ± 0.8	30.0 ± 1.5	0.73
18.0–18.1	15.8 ± 0.8	29.0 ± 1.5	0.74
18.1–18.2	15.0 ± 0.8	28.0 ± 1.5	0.74
18.2–18.3	14.3 ± 0.8	27.2 ± 1.6	0.75
18.3–18.4	13.8 ± 0.9	26.4 ± 1.6	0.76
18.4–18.5	13.3 ± 0.9	25.8 ± 1.7	0.77
18.5–18.6	13.0 ± 0.9	25.2 ± 1.8	0.77
18.6–18.7	12.6 ± 0.9	24.7 ± 1.8	0.78
18.7–18.8	12.4 ± 1.0	24.2 ± 1.9	0.78
18.8–18.9	12.2 ± 1.0	23.9 ± 2.0	0.79
18.9–19.0	12.0 ± 1.0	23.5 ± 2.0	0.79
19.0–19.1	11.8 ± 1.1	23.3 ± 2.1	0.79
19.1–19.2	11.7 ± 1.1	23.0 ± 2.1	0.79
19.2–19.3	11.6 ± 1.1	22.8 ± 2.2	0.79
19.3–19.4	11.5 ± 1.1	22.6 ± 2.2	0.79
19.4–19.5	11.4 ± 1.1	22.5 ± 2.2	0.79
19.5–19.6	11.4 ± 1.2	22.3 ± 2.3	0.79
$19.6 - \infty$	11.3 ± 1.2	22.1 ± 2.3	0.79

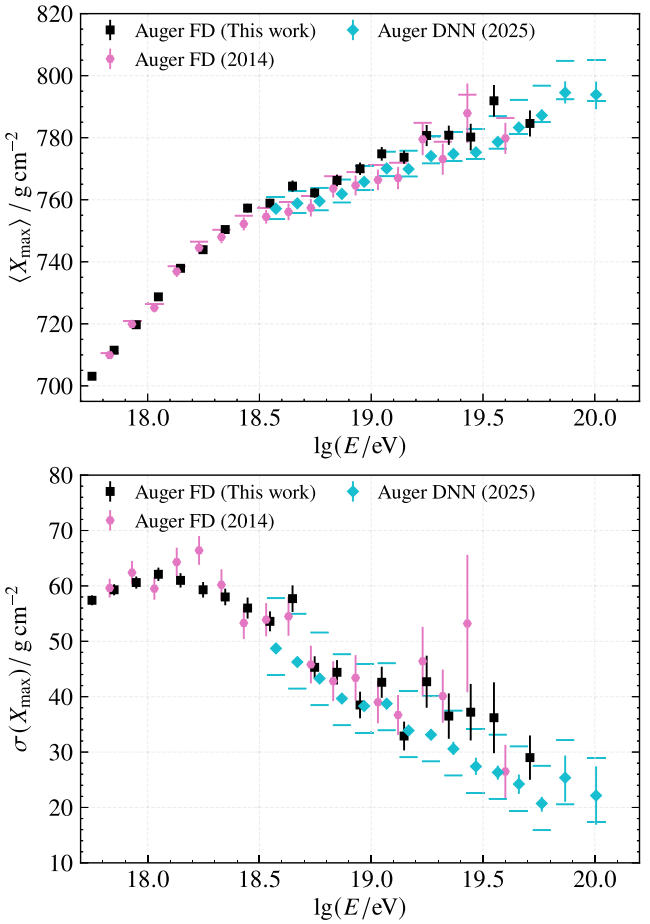


FIG. 21. $\langle X_{\text{max}} \rangle$ and $\sigma(X_{\text{max}})$ versus energy for different results produced by the Pierre Auger Collaboration, FD (2014) [16] and DNN (2025) [76]). Error bars denote the statistical uncertainties, while the horizontal caps indicate the uncorrelated systematic uncertainties.

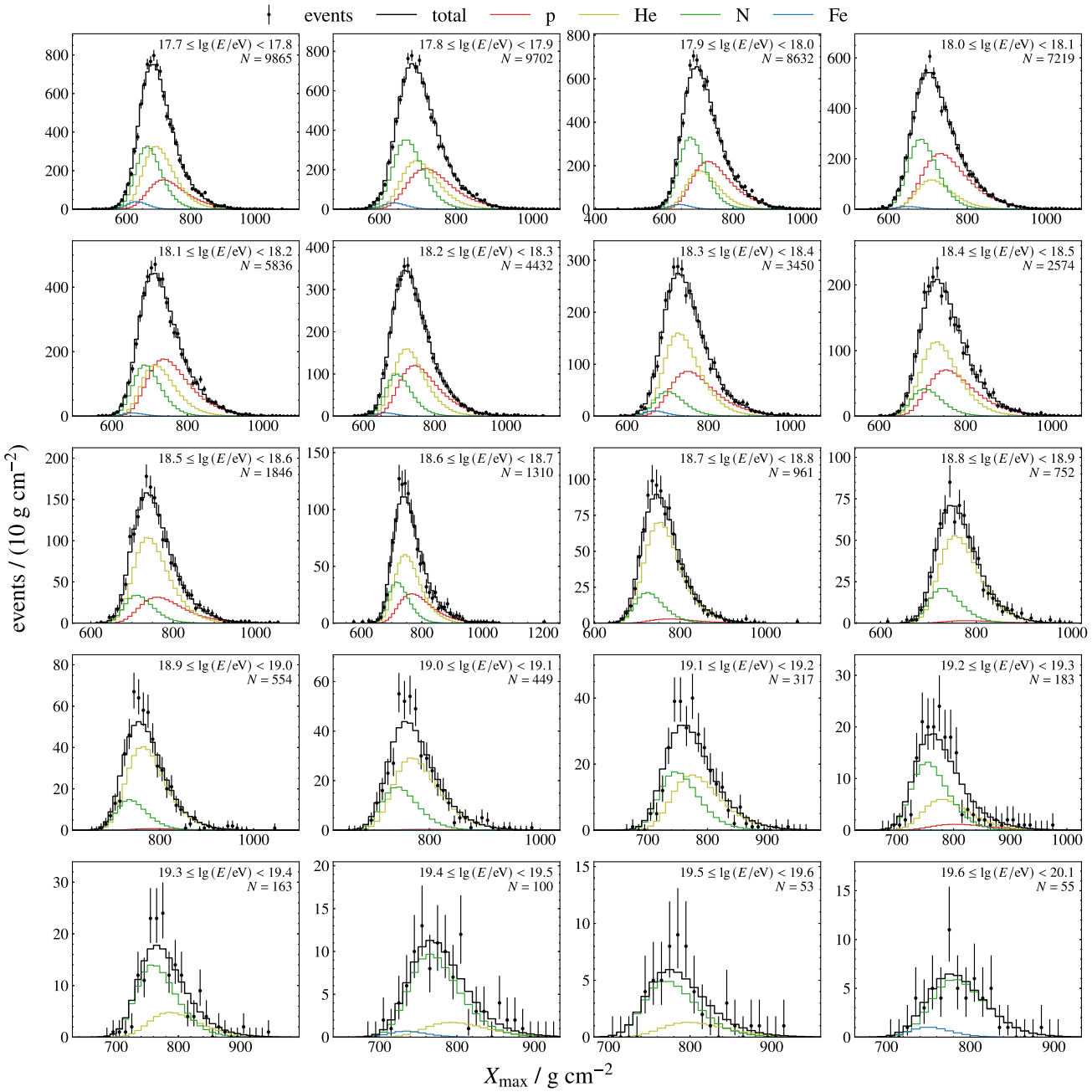


FIG. 22. Fits of composition fractions of the mass groups (H, He, N, Fe) with SIBYLL 2.3e in all energy bins: $X_{\max}$ distribution of the data (points with error bars) and composition templates (histograms).

The fit parameters are summarized in Table III together with their statistical uncertainties. Systematic uncertainties on p_i are estimated by assuming that the dominant uncertainty in the detector simulations is related to modeling the production and transmission of fluorescence light and the detector's optical response. This uncertainty is equal to the uncertainty of the Auger energy scale of 14%. A table of these parameters, including the fully correlated systematic uncertainties, can be found in Ref. [45].

2. Resolution

Table IV gives the parameters of $X_{\max}$ resolution, Eq. (4), including all effects discussed in Secs. IV B 1 and IV B 2.

APPENDIX C: COMPARISON OF $X_{\max}$ MOMENTS

In Fig. 21, we present the $\langle X_{\max}\rangle$ and $\sigma(X_{\max})$ moments obtained in this work and compare them to previous results

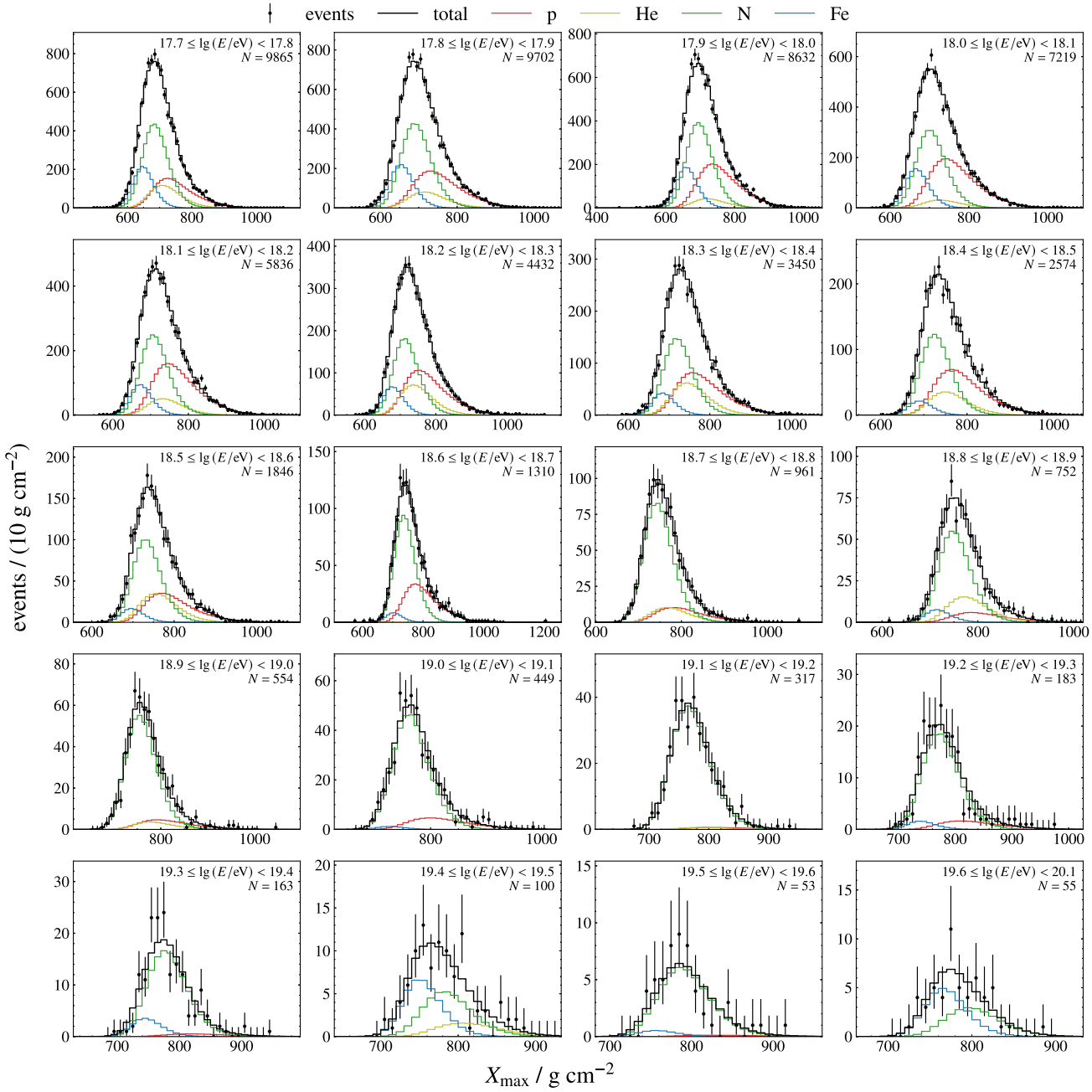


FIG. 23. Same as Fig. 22, but for EPOS LHC-R.

from the Pierre Auger Collaboration: the earlier FD $X_{\max}$ analysis ["FD (2014)" [16]] and the deep neural network analysis based on surface detector data ["DNN (2025)" [76]]. An energy-dependent $\langle X_{\max}\rangle$-difference is observed relative to these earlier results. The shift is expected from the improved aerosol treatment used in this analysis, in particular the correction for residual aerosol contamination in the clear reference nights used for data normalization [30]. Previously, this effect was accounted for as a systematic uncertainty and it is now corrected explicitly, resulting in shifted central values and reduced systematic uncertainties. Only the uncorrelated systematic uncertainties relevant for the relative comparison are shown. For FD (2014), this is the uncertainty associated with the VAOD treatment. For DNN (2025), the shown uncertainty is the quadratic sum of the same VAOD-related contribution, inherited through the calibration on FD data reconstructed prior to the aerosol-analysis update, and the uncorrelated uncertainty associated with the inference of $X_{\max}$ from the surface-detector data (see Fig. 11 of [76]).

Good agreement with FD (2014) is found for $\sigma(X_{\max})$. The fluctuations derived in the DNN (2025) analysis are

TABLE V. $\langle X_{\rm max}\rangle$ and $\sigma(X_{\rm max})$ with their statistical and systematic uncertainties. The third column shows the number of events N in each energy bin.

$\lg(E/\mathrm{eV})$	$\langle\lg(E/\mathrm{eV})\rangle$	N	$\langle X_{\rm max}\rangle/(\mathrm{g\,cm^{-2}})$	$\sigma(X_{\rm max})/(\mathrm{g\,cm^{-2}})$
[17.7, 17.8)	17.75	9865	$703.1 \pm 0.7^{+8.1}_{-10.2}$	$57.4 \pm 0.9^{+1.7}_{-1.6}$
[17.8, 17.9)	17.85	9702	$711.5 \pm 0.8^{+7.9}_{-10.2}$	$59.3 \pm 1.0^{+1.9}_{-1.7}$
[17.9, 18.0)	17.95	8632	$719.7 \pm 0.8^{+7.8}_{-10.2}$	$60.6 \pm 1.1^{+2.0}_{-1.8}$
[18.0, 18.1)	18.05	7219	$728.7 \pm 1.0^{+7.6}_{-10.2}$	$62.1 \pm 1.2^{+2.2}_{-1.9}$
[18.1, 18.2)	18.15	5836	$737.9 \pm 1.0^{+7.5}_{-10.1}$	$61.0 \pm 1.3^{+2.4}_{-2.1}$
[18.2, 18.3)	18.25	4432	$743.9 \pm 1.1^{+7.4}_{-9.9}$	$59.3 \pm 1.4^{+2.6}_{-2.2}$
[18.3, 18.4)	18.35	3450	$750.4 \pm 1.1^{+7.2}_{-9.7}$	$58.0 \pm 1.5^{+2.3}_{-2.0}$
[18.4, 18.5)	18.45	2574	$757.3 \pm 1.4^{+7.1}_{-9.4}$	$56.0 \pm 1.9^{+2.1}_{-1.8}$
[18.5, 18.6)	18.55	1846	$758.9 \pm 1.4^{+7.0}_{-9.1}$	$53.6 \pm 1.8^{+1.9}_{-1.7}$
[18.6, 18.7)	18.65	1310	$764.4 \pm 1.8^{+7.0}_{-8.8}$	$57.7 \pm 2.4^{+1.7}_{-1.5}$
[18.7, 18.8)	18.75	961	$762.2 \pm 1.6^{+6.9}_{-8.4}$	$45.3 \pm 2.0^{+1.5}_{-1.5}$
[18.8, 18.9)	18.85	752	$766.2 \pm 1.9^{+6.9}_{-8.1}$	$44.4 \pm 2.2^{+1.4}_{-1.4}$
[18.9, 19.0)	18.95	554	$770.0 \pm 2.0^{+6.9}_{-7.8}$	$38.5 \pm 2.4^{+1.4}_{-1.4}$
[19.0, 19.1)	19.05	449	$774.8 \pm 2.2^{+6.9}_{-7.5}$	$42.6 \pm 2.8^{+1.3}_{-1.3}$
[19.1, 19.2)	19.15	317	$773.7 \pm 2.1^{+6.9}_{-7.3}$	$32.9 \pm 2.6^{+1.3}_{-1.4}$
[19.2, 19.3)	19.25	183	$780.7 \pm 3.4^{+7.0}_{-7.2}$	$42.7 \pm 4.7^{+1.3}_{-1.3}$
[19.3, 19.4)	19.35	163	$780.8 \pm 3.1^{+7.0}_{-7.0}$	$36.5 \pm 4.1^{+1.3}_{-1.4}$
[19.4, 19.5)	19.44	100	$780.2 \pm 4.3^{+7.1}_{-7.0}$	$37.2 \pm 5.1^{+1.3}_{-1.5}$
[19.5, 19.6)	19.55	53	$791.9 \pm 5.1^{+7.1}_{-6.9}$	$36.2 \pm 6.4^{+1.4}_{-1.5}$
$[19.6, \infty)$	19.71	55	$784.6 \pm 4.2^{+7.2}_{-6.9}$	$29.0 \pm 4.0^{+1.6}_{-1.7}$

systematically smaller above $10^{19.2}$ eV than those found in this work, but are consistent within the systematic uncertainties of the DNN analysis, which amount to about $^{+7}_{-5}$ g cm^{-2}.

The UHE results reported by the Telescope Array Collaboration cannot be directly compared to ours, as their published $X_{\rm max}$ moments are not corrected for detector effects [60]. Instead, we refer to the results of the Auger-TA composition working group, which compares the data at detector level and finds good agreement between the two experiments [63]. A comparison to TA results below $10^{18.5}$ eV [79,80] remains to be carried out in a dedicated joint study.

APPENDIX D: FITS OF COMPOSITION FRACTIONS TO $X_{\rm max}$ DISTRIBUTIONS

The fitted $X_{\rm max}$ distributions in each energy bin are shown in Figs. 22 and 23 for the SIBYLL 2.3e and EPOS LHC-R hadronic interaction models.

APPENDIX E: MOMENTS OF THE $X_{\rm max}$ DISTRIBUTION

The bias- and resolution-corrected $X_{\rm max}$ moments derived in this analysis are listed in Table V together with their statistical and systematic uncertainties.

[1] N. Globus and R. D. Blandford, Ultrahigh-energy cosmic rays, Annu. Rev. Astron. Astrophys. **63**, 339 (2025).

[2] K. Greisen, Cosmic Ray Showers, Annu. Rev. Nucl. Part. Sci. **10**, 63 (1960).

[3] J. Linsley and A. A. Watson, Validity of scaling to 10^{20} eV and high-energy cosmic-ray composition, Phys. Rev. Lett. **46**, 459 (1981).

[4] J. Engel *et al.*, Nucleus-nucleus collisions and interpretation of cosmic-ray cascades, Phys. Rev. D **46**, 5013 (1992).

[5] J. Matthews, A Heitler model of extensive air showers, Astropart. Phys. **22**, 387 (2005).

[6] K.-H. Kampert and M. Unger, Measurements of the cosmic ray composition with air shower experiments, Astropart. Phys. **35**, 660 (2012).

[7] P. Abreu *et al.* (Pierre Auger Collaboration), Interpretation of the depths of maximum of extensive air showers measured by the pierre auger observatory, J. Cosmol. Astropart. Phys. 02 (2013) 026.

[8] S. Ostapchenko, Total and diffractive cross sections in enhanced Pomeron scheme, Phys. Rev. D **81**, 114028 (2010).

[9] T. Pierog *et al.*, EPOS LHC: Test of collective hadronization with data measured at the CERN Large Hadron Collider, Phys. Rev. C **92**, 034906 (2015).

[10] F. Riehn *et al.*, Hadronic interaction model Sibyll 2.3d and extensive air showers, Phys. Rev. D **102**, 063002 (2020).

[11] S. Ostapchenko, QGSJET-III model of high energy hadronic interactions. II. Particle production and extensive air shower characteristics, Phys. Rev. D **109**, 094019 (2024).

[12] T. Pierog and K. Werner, EPOS LHC-R: Up-to-date hadronic model for EAS simulations, Proc. Sci. ICRC2023 (**2023**) 230.

[13] J. Albrecht *et al.*, Global tuning of hadronic interaction models with accelerator-based and astroparticle data, Nat. Rev. Phys. **8**, 98 (2026).

[14] A. Aab *et al.* (Pierre Auger Collaboration), The Pierre Auger cosmic ray observatory, Nucl. Instrum. Methods Phys. Res., Sect. A **798**, 172 (2015).

[15] J. Abraham *et al.* (Pierre Auger Collaboration), Measurement of the depth of maximum of extensive air showers above 10^{18} eV, Phys. Rev. Lett. **104**, 091101 (2010).

[16] A. Aab *et al.* (Pierre Auger Collaboration), Depth of maximum of air-shower profiles at the Pierre Auger Observatory. I. Measurements at energies above $10^{17.8}$ eV, Phys. Rev. D **90**, 122005 (2014).

[17] A. Aab *et al.* (Pierre Auger Collaboration), Depth of maximum of air-shower profiles at the Pierre Auger Observatory. II. Composition implications, Phys. Rev. D **90**, 122006 (2014).

[18] A. Aab *et al.* (Pierre Auger Collaboration), The Pierre Auger Observatory Upgrade—Preliminary Design Report, arXiv: 1604.03637.

[19] I. Allekotte *et al.* (Pierre Auger Collaboration), The surface detector system of the Pierre Auger Observatory, Nucl. Instrum. Methods Phys. Res., Sect. A **586**, 409 (2008).

[20] J. Abraham *et al.* (Pierre Auger Collaboration), The fluorescence detector of the Pierre Auger Observatory, Nucl. Instrum. Methods Phys. Res., Sect. A **620**, 227 (2010).

[21] J. Abraham *et al.* (Pierre Auger Collaboration), Properties and performance of the prototype instrument for the Pierre Auger Observatory, Nucl. Instrum. Methods Phys. Res., Sect. A **523**, 50 (2004).

[22] F. Sanchez *et al.* (Pierre Auger Collaboration), The AMIGA detector of the Pierre Auger Observatory, in *Proceedings of the 32nd ICRC*, (Beijing, China, 2011), 3, 149.

[23] H.-J. Mathes *et al.* (Pierre Auger Collaboration), The HEAT Telescopes of the Pierre Auger Observatory—Status and First Data, *Proceedings of the 32nd ICRC*, (Beijing, China, 2011), 3, 153.

[24] J. T. Brack *et al.*, Absolute photometric calibration of large aperture optical systems, Astropart. Phys. **20**, 653 (2004).

[25] A. C. Rovero *et al.*, Multi-wavelength calibration procedure for the Pierre Auger Observatory Fluorescence Detectors, Astropart. Phys. **31**, 305 (2009).

[26] J. T. Brack *et al.*, Absolute calibration of a large-diameter light source, J. Instrum. **8**, P05014 (2013).

[27] P. Abreu *et al.* (Pierre Auger Collaboration), Description of atmospheric conditions at the Pierre Auger Observatory using the Global Data Assimilation System (GDAS), Astropart. Phys. **35**, 591 (2012).

[28] B. Fick *et al.*, The central laser facility at the Pierre Auger Observatory, J. Instrum. **1**, P11003 (2006).

[29] J. Abraham *et al.* (Pierre Auger Collaboration), A study of the effect of molecular and aerosol conditions in the atmosphere on air fluorescence measurements at the Pierre Auger Observatory, Astropart. Phys. **33**, 108 (2010).

[30] V. M. Harvey *et al.* (Pierre Auger Collaboration), A new cross-check and review of aerosol attenuation measurements at the Pierre Auger Observatory, EPJ Web Conf. **444**, 300 (2023).

[31] J. Chirinos *et al.* (Pierre Auger Collaboration), Cloud Monitoring at the Pierre Auger Observatory, in *Proceedings of the 33rd ICRC*, (Rio de Janeiro, Brazil, 2013), 33, 2244.

[32] P. Abreu *et al.* (Pierre Auger Collaboration), Identifying clouds over the Pierre Auger Observatory using infrared satellite data, Astropart. Phys. **50–52**, 92 (2013).

[33] P. Sommers, Capabilities of a giant hybrid air shower detector, Astropart. Phys. **3**, 349 (1995).

[34] B. R. Dawson, H. Y. Dai, P. Sommers, and S. Yoshida, Simulations of a giant hybrid air shower detector, Astropart. Phys. **5**, 239 (1996).

[35] A. N. Bunner, K. Greisen, and P. B. Landecker, An imaging system for EAS optical emission, Can. J. Phys. Suppl. **46**, 266 (1968).

[36] M. Risse and D. Heck, Energy release in air showers, Astropart. Phys. **20**, 661 (2004).

[37] M. Unger, B. R. Dawson, R. Engel, F. Schussler, and R. Ulrich, Reconstruction of longitudinal profiles of Ultra-High energy cosmic ray showers from fluorescence and cherenkov light measurements, Nucl. Instrum. Methods Phys. Res., Sect. A **588**, 433 (2008).

[38] T. K. Gaisser and A. M. Hillas, Reliability of the Method of Constant Intensity Cuts for Reconstructing the Average Development of Vertical Showers, in *Proceedings of the 15th ICRC*, (Plovdiv, Bulgaria, 1977), 8, 353.

[39] S. Andringa, R. Conceicao, and M. Pimenta, Mass composition and cross-section from the shape of cosmic ray shower longitudinal profiles, Astropart. Phys. **34**, 360 (2011).

[40] J. Bellido *et al.* (Pierre Auger Collaboration), The fitting procedure for longitudinal shower profiles observed with the fluorescence detector of the Pierre Auger Observatory, Proc. Sci. ICRC2023 (**2023**) 211.

[41] A. Aab *et al.* (Pierre Auger Collaboration), Data-driven estimation of the invisible energy of cosmic ray showers with the Pierre Auger Observatory, Phys. Rev. D **100**, 082003 (2019).

[42] A. Aab *et al.* (Pierre Auger Collaboration), Measurement of the cosmic-ray energy spectrum above 2.5×10^{18} eV using the Pierre Auger Observatory, Phys. Rev. D **102**, 062005 (2020).

[43] P. Abreu *et al.* (Pierre Auger Collaboration), The lateral trigger probability function for the ultra-high energy cosmic ray showers detected by the Pierre Auger Observatory, Astropart. Phys. **35**, 266 (2011).

[44] V. M. Harvey *et al.* (Pierre Auger Collaboration), Real-Time measurements with atmospheric instruments at the pierre auger observatory, Proc. Sci., ICRC2019 (**2021**) 283.

[45] Pierre Auger Collaboration, Supplementary data and tables on zenodo (2026), 10.5281/zenodo.18024023.
[46] P. Abreu *et al.* (Pierre Auger Collaboration), The exposure of the hybrid detector of the Pierre Auger Observatory, Astropart. Phys. **34**, 368 (2011).
[47] E. Santos *et al.* (Pierre Auger Collaboration), Update on the offline framework for AugerPrime and production of reference simulation libraries using the VO auger grid resources, Proc. Sci. ICRC2023 (**2023**) 248.
[48] T. Bergmann *et al.*, One-dimensional hybrid approach to extensive air shower simulation, Astropart. Phys. **26**, 420 (2007).
[49] M. Bleicher *et al.*, Relativistic hadron hadron collisions in the ultrarelativistic quantum molecular dynamics model, J. Phys. G **25**, 1859 (1999).
[50] S. Argiro *et al.* (Pierre Auger Collaboration), The offline software framework of the Pierre Auger Observatory, Nucl. Instrum. Methods Phys. Res. **580**, 1485 (2007).
[51] A. Aab *et al.* (Pierre Auger Collaboration), Measurement of the average shape of longitudinal profiles of cosmic-ray air showers at the Pierre Auger Observatory, J. Cosmol. Astropart. Phys. 03 (2019) 018.
[52] O. Tkachenko *et al.* (Pierre Auger Collaboration), Measurement of the inelastic proton-proton cross-section at $\sqrt{s} \geq$ 40 TeV using the hybrid data of the Pierre Auger Observatory, Proc. Sci. ICRC2025 (**2025**) 416.
[53] P. Abreu *et al.* (Pierre Auger Collaboration), Techniques for measuring aerosol attenuation using the Central Laser Facility at the Pierre Auger Observatory, J. Instrum. **8**, P04009 (2013).
[54] M. Ave *et al.* (AIRFLY Collaboration), Precise measurement of the absolute fluorescence yield of the 337 nm band in atmospheric gases, Astropart. Phys. **42**, 90 (2013).
[55] K. Louedec and J. Colombi, Atmospheric multiple scattering of fluorescence light from extensive air showers and effect of the aerosol size on the reconstruction of energy and depth of maximum, Astropart. Phys. **57–58**, 6 (2014).
[56] S. Baker and R. D. Cousins, Clarification of the use of chi square and likelihood functions in fits to histograms, Nucl. Instrum. Methods **221**, 437 (1984).
[57] B. Dawson *et al.* (Pierre Auger Collaboration), The energy scale of the Pierre Auger Observatory, Proc. Sci., ICRC2019 (**2020**) 231.
[58] A. Abdul Halim *et al.* (Pierre Auger Collaboration), Testing hadronic-model predictions of depth of maximum of air-shower profiles and ground-particle signals using hybrid data of the Pierre Auger Observatory, Phys. Rev. D **109**, 102001 (2024).
[59] C. M. Schäfer *et al.* (Pierre Auger Collaboration), A novel tool for the absolute end-to-end calibration of fluorescence telescopes—the XY-scanner, EPJ Web Conf. **444**, 305 (2023).
[60] R. U. Abbasi *et al.* (Telescope Array Collaboration), Depth of ultra high energy cosmic ray induced air shower maxima measured by the telescope array black rock and long ridge FADC fluorescence detectors and surface array in hybrid mode, Astrophys. J. **858**, 76 (2018).
[61] F. J. Massey, The Kolmogorov-Smirnov test for goodness of fit, J. Am. Stat. Assoc. **46**, 68 (1951).
[62] F. W. Scholz and M. A. Stephens, K-Sample Anderson–Darling tests, J. Am. Stat. Assoc. **82**, 918 (1987).
[63] A. Yushkov *et al.* (Pierre Auger and Telescope Array Collaborations), Depth of maximum of air-shower profiles: Testing the compatibility of the measurements at the Pierre Auger Observatory and the Telescope Array, Proc. Sci. ICRC2023 (**2023**) 249.
[64] A. Abdul Halim *et al.* (Pierre Auger Collaboration), Energy spectrum of ultrahigh-energy cosmic rays across declinations −90° to +44.8° as measured at the Pierre Auger Observatory, Phys. Rev. Lett. **135**, 241002 (2025).
[65] A. Abdul Halim *et al.* (Pierre Auger Collaboration), Inference of the mass composition of cosmic rays with energies from $10^{18.5}$ to 10^{20} eV using the Pierre Auger Observatory and Deep Learning, Phys. Rev. Lett. **134**, 021001 (2025).
[66] A. A. Watson, The mass of cosmic rays of ultra-high energy, Astropart. Phys. **176**, 103200 (2026).
[67] J. Linsley, Spectra, anisotropies and composition of cosmic rays above 1000 GeV, in *Proceedings of the 18th ICRC*, (Bangalore, India, 1983), 12, 135.
[68] C. Evoli, I. Vaiman, S. Petrera, and F. Salamida, Updated air-shower xmax moment parametrizations for UHECR composition with latest hadronic interaction models, Astropart. Phys. **179**, 103239 (2026).
[69] D. Foreman-Mackey, D. W. Hogg, D. Lang, and J. Goodman, emcee: The MCMC hammer, Publ. Astron. Soc. Pac. **125**, 306 (2013).
[70] G. R. Farrar, Particle physics at ultrahigh energies, in *18th International Symposium on Very High Energy Cosmic Ray Interactions*, (Geneva, Switzerland, 2014), arXiv:1902.11271.
[71] V. Pavlidou and T. Tomaras, What do the highest-energy cosmic-ray data suggest about possible new physics around 50 TeV?, Phys. Rev. D **99**, 123016 (2019).
[72] A. Aab *et al.* (Pierre Auger Collaboration), Evidence for a mixed mass composition at the "ankle" in the cosmic-ray spectrum, Phys. Lett. B **762**, 288 (2016).
[73] J. Vicha *et al.* (Pierre Auger Collaboration), Update on testing of air-shower modelling using combined data of the pierre auger observatory and phenomenological consequences, Proc. Sci. ICRC2025 (**2025**) 431 [arXiv:2507.09802].
[74] A. Yushkov *et al.* (Pierre Auger Collaboration), Constraints on the spread of nuclear masses in ultra-high-energy cosmic rays based on the phase I hybrid data from the Pierre Auger Observatory, Proc. Sci. ICRC2025 (**2025**) 442.
[75] A. Aab *et al.* (Pierre Auger Collaboration), Inferences on mass composition and tests of hadronic interactions from 0.3 to 100 EeV using the water-Cherenkov detectors of the Pierre Auger Observatory, Phys. Rev. D **96**, 122003 (2017).
[76] A. Abdul Halim *et al.* (Pierre Auger Collaboration), Measurement of the depth of maximum of air-shower profiles with energies between $10^{18.5}$ and 10^{20} eV using the surface detector of the Pierre Auger Observatory and Deep Learning, Phys. Rev. D **111**, 022003 (2025).
[77] M. Stadelmaier *et al.* (Pierre Auger Collaboration), Reconstructing air-shower observables using a universality-based model, Proc. Sci., UHECR2024 (**2025**) 117.

[78] The Pierre Auger Collaboration10.5281/zenodo.18024023.
[79] R. U. Abbasi *et al.* (Telescope Array Collaboration), The cosmic-ray composition between 2 PeV and 2 EeV observed with the TALE detector in monocular mode, Astrophys. J. **909**, 178 (2021).
[80] R. U. Abbasi *et al.* (Telescope Array Collaboration), Cosmic ray mass composition measurement in the energy range from $10^{16.5}$ eV to $10^{18.5}$ eV observed with the TALE hybrid detector, Phys. Rev. D **113**, 062003 (2026).